Physics – Uspekhi **60** (2) 187 – 203 (2017)

INSTRUMENTS AND METHODS OF INVESTIGATION PACS numbers: 07.85.Tt, **41.50.+h**

X-ray microscopy

V V Lider

DOI: https://doi.org/10.3367/UFNe.2016.06.037830

Contents

Abstract. X-ray microscopy is a technique for obtaining real-space two- or three-dimensional images of an object using elements of the focusing optics. In this paper, various types of microscopes are reviewed and their applicability is examined; methods for obtaining image contrast are discussed, and avenues for the further development of X-ray microscopy are outlined.

Keywords: X-rays, X-ray optics, microscopy, spectroscopy, topography, fluorescence, magnetic dichroism

1. Introduction

X-ray microscopy is the collection of methods for investigating the microscopic structure of objects with the aid of X-ray radiation. These methods, which employ focusing optical elements, permit obtaining magnified images of an object under investigation in real space.

Owing to their short wavelength, X-rays penetrate a sample to a far greater depth than visible light. Consequently, they may be used to study the internal structure of objects opaque to visible light. X-ray microscopy may reach the diffraction-limited resolution on the order of several dozen nanometers and occupies an intermediate position between optical and electron microscopy.

However, electron microscopy, which offers a higher resolution, is not a nondestructive investigation technique and requires a vacuum and samples with metallic or metallized surfaces.

The majority of X-ray lensless methods for the microstructure investigation of a studied object [1, 2] produce its image in the reciprocal space, which calls for the use of mathematical inversion for reconstructing the real image, which is often responsible for the emergence of different artifacts. The resolution of these methods is limited, as a rule, by the size of the X-ray radiation source, which does not exceed a submicrometer level. The use of lenses in X-ray microscopes makes it possible to form a demagnified source image and reduce its dimension to several dozen nanometers.

X-ray microscopy, which permits carrying out research at a new structural level, is finding increasing application along with optical and electron microscopies. The emergence of a large number of reviews dedicated to different aspects of this method demonstrates that X-ray microscopy is popular among researchers. For instance, the past ten years have seen more than 20 reviews [3–24] which consider the use of X-ray microscopy for investigations in the area of biomedicine [9–11], materials science [12–22] (including polymer [18, 19] and magnetic material [20–22] studies), as well as the environment [10, 12, 23, 24].

This review is an attempt to describe the main characteristics and features of X-ray microscopy, as well as the feasibility of using it to investigate the morphology and internal structure of organic and inorganic samples with submicrometer resolution.

V V Lider Federal Scientific Research Center
'Crystallography and Photonics', Russian Academy of Sciences,
Shubnikov Institute of Crystallography,
Leninskii prosp. 59, 119333 Moscow, Russian Federation
E-mail: lider@ns.crys.ras.ru, vallider@yandex.ru

Received 25 April 2016, revised 30 May 2016
Uspekhi Fizicheskikh Nauk **187** (2) 201 – 219 (2017)
DOI: https://doi.org/10.3367/UFNr.2016.06.037830
Translated by E N Ragozin; edited by A Radzig

2. X-ray microscope types: field-of-view X-ray microscope and scanning X-ray microscope

There are two main types of transmission X-ray microscopes: conventional transmission X-ray microscopes (TXMs), which are often referred to as field-of-view X-ray microscopes, and scanning transmission X-ray microscopes (STXMs).

The optical configuration of a TXM (Fig. 1a) bears much resemblance to that of a conventional light microscope. The TXM consists of a condenser and an objective lens. The latter produces a magnified image of a sample in the detection plane, which is recorded with a pixel detector (a charge-coupled device (CCD) is commonly employed for this purpose).

In an STXM (Fig. 1b), an objective lens focuses an X-ray beam onto a small-sized spot on the sample, the sample is raster-scanned, and the output intensity is recorded with a detector for each scan position. In the majority of STXMs, use is made of detectors without spatial resolution, which integrate the radiation transmitted through the sample [23, 25].

The history of the origin and development of X-ray microscopy was set out in detail in review [26]. We note that the function of a source in the first TXMs [4] and STXMs [27] was fulfilled by synchrotron radiation (SR). Owing to their properties (high brightness, broad energy range, polarization, temporal structure), SR sources are the sources of choice for the majority of X-ray microscopes in existence today. However, interest is growing in so-called compact instruments, which take advantage of laser-generated plasma radiation [28–30] and X-ray tubes with a rotating anode [31] or a microfocus [8, 32, 33]. Owing to their small sizes, such instruments may be accommodated on an optical table, thereby permitting experiments to be carried out in laboratory conditions. However, due to the distinct nature of characteristic emission lines, these instruments lack the energy flexibility required for realizing some important applications of spectroscopy like X-ray absorption spectroscopy. Nevertheless, plasma sources which utilize liquid nitrogen as the target are suited to the laboratory X-ray microscopy of biological objects thanks to the high-intensity emission at wavelengths of 2.478 and 2.879 nm, which are in the so-called water window domain, where X-ray absorption by proteins is an order of magnitude stronger than X-ray absorption by water.

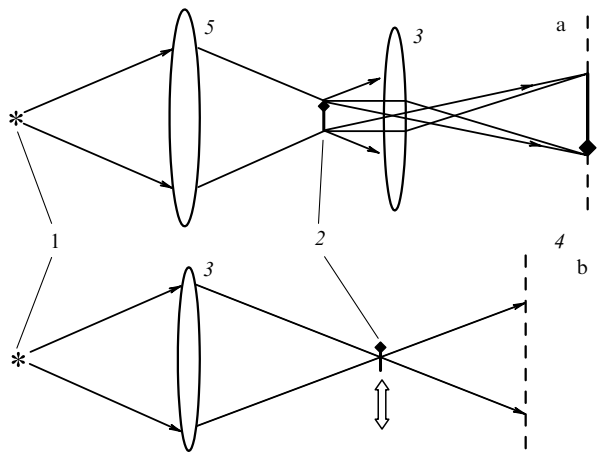

Figure 1. Optical configurations of a TXM (a) and an STXMs (b): *1* — radiation source, *2* — sample under investigation, *3* — objective lens, *4* — detection plane, and *5* — condenser.

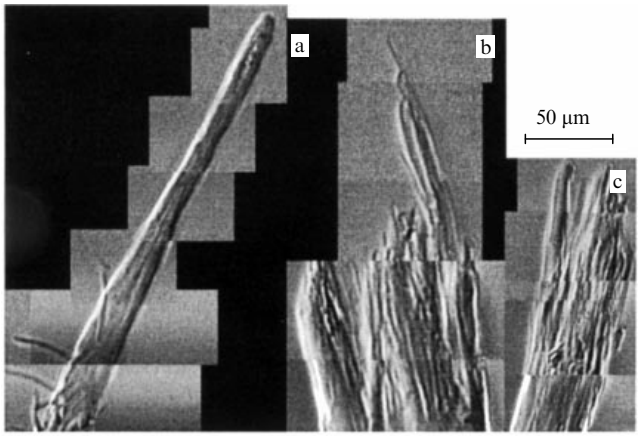

Figure 2. TXM images of the hair tips of (a) 22-, (b) 28-, and (c) 32-year-old women [34].

TXMs and STXMs are commonly considered complementary techniques; they are about equally popular and each offers its own important advantages. Like other scanning probe instruments, STXMs permit simultaneous monitoring of various signals with the use of the corresponding X-ray and electron detectors. It is therefore possible to simultaneously record X-ray images and fluorescence emission photons. That is why the scanning instruments are well suited to combine imaging and spectroscopy measurements even for a fixed X-ray energy [5].

The use of an STXM permits obtaining images of arbitrary size, while with a TXM, where the condenser commonly illuminates a field 10–50 μm in diameter, large image fields may be obtained only by 'stitching' several images (Fig. 2). On the other hand, the simultaneous illumination of all elements of a sample makes it possible to obtain images with a single high-intensity pulse.

The main disadvantage of an STXM in comparison with a TXM is its low data acquisition rate. The typical exposure time required to obtain an STXM image amounts to several minutes, whereas the TXM exposure time is on the order of several seconds. With an increase in exposure time, problems like beam instability, vibration, and thermal drift become significant for the STXM, with the result that TXM images may practically offer a higher spatial resolution. For the STXM image resolution to be determined by the probe size, the sample should be moved with shorter increments than the probe size. This may be achieved with the employment of piezoelectric transducers with one feedback mechanism or another [35].

3. Focusing X-ray optics for X-ray microscopy

3.1 Objective lens. Fresnel zone plate

Fresnel zone plates (FZPs) as X-ray optical elements were proposed by Baez [36] in 1952. FZPs offer the highest spatial resolution of all X-ray optical elements reliant on diffraction; however, FZP imaging encounters a variety of problems, which are solved by making a multitude of modifications of the basic model [37].

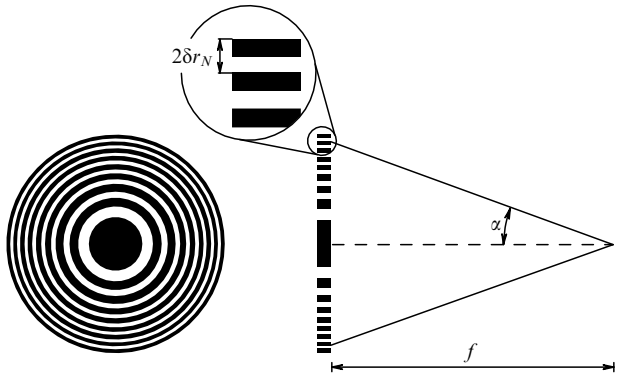

Figure 3. Schematic diagram of an FZP: δr_N is the outer zone width, α is the largest diffraction angle, and f is the focal length.

A FZP is composed of a series of concentric annular zones (Fig. 3) which alternately absorb and transmit radiation. The focusing effect is produced by the interference of the waves transmitted through the nonabsorbing zones.

Since a zone plate is a special case of a diffraction grating, higher-order foci would be expected to exist. In every transmitting (or absorbing) domain of the zone plate, there are m Fresnel zones which result in the mutual cancellation of perturbations, when m is an even number. That is why the resultant focus exists only when m is odd. Therefore, there is an infinite number of positive and negative foci for $m = \pm 1$, ± 3, ± 5, ... Furthermore, some part of the radiation does not experience diffraction, which corresponds to $m = 0$.

The diffraction properties of zone plates and their employment in X-ray microscopes are described in Refs [38–41] and numerous references cited therein.

The zone's radii are defined by the formula [38]

$$r_n^2 = mn\lambda f_m + \frac{m^2 n^2 \lambda^2}{4} \approx mn\lambda f_m \,, \tag{1}$$

where r_n is the nth zone radius, λ is the wavelength, m is the diffraction order, and f_m is the focal length:

$$f_m = \frac{D\delta r_N}{\lambda m} = \frac{D^2}{4\lambda N m} \,. \tag{2}$$

Here, δr_N is the outer zone width, D is the FZP diameter, and N is the total number of zones. From formula (2) it follows that the FZP diameter depends on the outer zone width and the number of zones:

$$D = 4N\delta r_N \,. \tag{3}$$

Typical zone plates measure $\approx$ 120–240 μm in diameter and contain from 100 to 1000 zones, while the outer zone width ranges from 20 to 50 nm [23].

FZPs operate as thin lenses and therefore offer diffraction-limited lateral spatial resolution d_m:

$$d_m = \frac{0.61\lambda}{\mathrm{NA}} \,, \tag{4}$$

which was calculated by Rayleigh for a lens with a numerical aperture (NA). The magnitude of NA is defined by the largest diffraction angle α (see Fig. 3), which in turn is expressed in terms of the outer zone width, the wavelength, and the diffraction order:

$$\mathrm{NA} = \sin\alpha = \frac{m\lambda}{2\delta r_N} \,. \tag{5}$$

Two more useful expressions may be derived from expressions (4) and (5). One of them is the relation between the outer zone width δr_N of the N-zone plate and the Rayleigh resolution limit:

$$d_m = \frac{1.22\,\delta r_N}{m} \,. \tag{6}$$

The focal dimension d of the mth diffraction order is defined by the Rayleigh diffraction resolution limit d_m, the geometrically demagnified source size d_r, as well as the chromatic aberration d_c:

$$\begin{aligned} d &= (d_m^2 + d_\mathrm{r}^2 + d_\mathrm{c}^2)^{1/2} \\ &= \left[\left(\frac{1.22\,\delta r_N}{m}\right)^2 + d_\mathrm{r}^2 + D^2\left(\frac{\Delta\lambda}{\lambda}\right)^2\right]^{1/2} , \end{aligned} \tag{7}$$

where $\Delta\lambda/\lambda$ is the relative width of the primary beam spectrum, and d_r is a function dependent on the experiment geometry. For an STXM, $d_\mathrm{r} = sq/p$, where s is the source size, p is the source–FZP distance, and q is the FZP–sample distance. For a TXM, d_r depends on the detector geometry and pixel size Δ: $d_\mathrm{r} = \Delta/(Vm)$, where V is the magnification of objective FZP [39].

By putting $sq/p \approx \lambda f_m/l_\mathrm{coh}$ (where l_coh is the transverse beam coherence) and using formula (3), we bring expression (7) for an STXM to the following form:

$$d = \frac{1.22\delta r_N}{m}\left[1 + \left(\frac{D}{1.22 l_\mathrm{coh}}\right)^2 + (3.28Nm)^2\left(\frac{\Delta\lambda}{\lambda}\right)^2\right]^{1/2} . \tag{8}$$

As follows from formula (8), attaining the diffraction resolution limit requires that the STXM objective be illuminated by a coherent beam with a monochromaticity no worse than the reciprocal of the product of the total number of zones and the diffraction order: $\Delta\lambda/\lambda \leqslant (mN)^{-1}$ [39]. That is why STXMs operate better with beams emanating from undulators [10, 40].

In a TXM, all elements of the object are illuminated, and they are simultaneously imaged by a pixel detector. Every element of the field is independently visualized when the object is irradiated by an incoherent or partially coherent beam. Consequently, the bending magnet of a synchrotron storage ring or laboratory sources are better suited for the TXM than an undulator source [5]. Moreover, the operation with a highly coherent beam may give rise to spotty patterns (speckles) on the image [42]. For the purpose of lowering the spatial coherence, the authors of Ref. [43] placed a diffuser in front of the sample.

Therefore, a zone plate with a small width of the outer zone can provide a good spatial resolution. Furthermore, owing to a higher diffraction order m, the spatial resolution may be improved by a factor of m. A high image resolution with the use of third-order diffraction was experimentally demonstrated for 'hard' X-rays (with a photon energy $E > 1$ keV) [44–46]. A disadvantage of the images obtained using high diffraction order is an m^2-fold increase in exposure time, because the diffraction efficiency Q is inversely proportional to m^2: $Q = 1/(m\pi)^2$ [41]. The zone plate efficiency is determined by the fraction of X-rays incident on the optical

element, which are focused into the desired diffraction order. Ideally, the efficiency of a simple FZP in the first diffraction order is equal to π^{-2}, or about 10%. The remaining part of the radiation is absorbed (50%) or goes into other diffraction orders: the zeroth (25%), negative (12.5%), and high positive (2.5%) orders [47].

To extract the first order and reject the undesired zeroth and high diffraction orders, the zone plate of an STXM is often equipped with a central stop in combination with a collimating opening (order-sorting aperture) near the FZP focal plane (Fig. 4). For a TXM, the zero-order diffraction beam is eliminated by placing a stop at the condenser center or immediately behind it.

Due to the structural features of the microscopes (in a TXM, the studied sample is placed in front of the objective FZP and behind it in an STXM), the low FZP efficiency has the effect that the sample in the STXM is subjected to a much lower radiation load than in the TXM.

Another important parameter of X-ray microscopes is the depth of focus (DOF) [48]:

$$\mathrm{DOF} = \pm\frac{\lambda}{2}\,(\mathrm{NA})^2 = \pm\frac{2(\delta r_N)^2}{m^2\lambda}\,. \qquad (9)$$

The theoretically evaluated DOF of an FZP with a diameter of 135 μm and an outer zone width of 35 nm is equal to 2.1 μm for soft X-ray radiation in the 528–540 eV energy range [49], while its corresponding value for a TXM operating with hard X-rays ($E = 8$ keV) amounts to about 40 μm [50]. The necessity of X-ray studies of 'thick' samples invites the expansion of the usage of hard X-ray radiation. 'Hard' X-ray microscopy furnishes a unique possibility of studying materials on a nanometer scale and provides a set of methods like fluorescence, differential phase contrast, and spectroscopy. All these analytical methods complement each other and provide a complex map of structural, chemical, and elemental properties of the sample. Attaining a sufficiently high spatial resolution and contrast ratio calls for high-efficiency nanofocusing optics to form a beam focal spot of minimal size and provide the requisite X-ray photon density.

Expertise has been accumulated in the fabrication of FZPs which efficiently focus soft ($E < 1$ keV) X-ray radiation and provide a spatial resolution of 15–30 nm [51–53]. Improvement in the spatial resolution without a sacrifice in efficiency is impeded by the necessity to fabricate FZPs which combine a small outer zone width δr_N with a large thickness (relief depth) T for attaining a high aspect ratio $T/\delta r_N$.

Electron-beam lithography with subsequent etching [54] remains the most successful technique of FZP fabrication to date. Nevertheless, the small width of the outer zone, which determines the zone plate resolution, is limited by the minimal diameter of the electron beam, the effect of electron scattering, and the generation of secondary electrons during the electron beam lithography. The achievable aspect ratio is limited by the procedure of dry etching, since this process is not perfectly anisotropic in the preparation of narrow nanostructures [55]. That is why methods aimed at increasing the thickness (relief depth) of an FZP show the greatest promise for the fabrication of FZPs with a high aspect ratio. Several methods [55–58] have been developed to solve this problem, but so far they have been infrequently used.

Unlike the above techniques, the sputtered-sliced (or 'jelly-roll') zone plate method proposed by the authors of Ref. [59] has gained wide acceptance. FZPs are produced here by alternately coating a cylindrical microwire with a multilayer structure composed of two materials with different X-ray absorption or with different properties of the phase shift, depending on the requisite zone plate structure, with the subsequent slicing of the structure into fragments of requisite thickness using a focused ion beam. In principle, the zone widths may range down to several atomic layers and, furthermore, there are no limitations on the aspect ratio in this case [60]. This method may be employed to fabricate X-ray optical components providing a resolution of better than 10 nm. However, the theoretical resolution limit may prove to be unattainable due to the aberrations arising from zone positioning errors, which affect the focal spot size.

The accuracy of layer deposition for FZPs with a focal length suited to practical application is a serious problem. The practical difficulties associated with the wire shape, the interlayer roughness of the multilayer structure, and the deformations in the course of its slicing hinder the fabrication of high-resolution FZPs by this method. In the view of the authors of Ref. [61], the problem may be solved by *in situ* layer thickness measurements in the course of fabrication. In this case, the zone thickness may be corrected during FZP fabrication, which will help eliminate positioning errors and correct the layer deposition rate. In doing this, the measurement uncertainty of the layer thickness of a zone plate may not exceed a half of the outer zone width.

To produce FZPs by this method, researchers tested a broad set of 'contrasting' materials with a high thermal endurance and a small diffusion coefficient: Al/Cu [62], Al_2O_3/Ta_2O_5 [63], Al_2O_3/HfO_2 [64], $Ni_{80}Cr_{20}/SiO_2$ [65], $SiO_2/Si_{1-x}Ge_xO_2$ [66].

The efficiency of FZPs made by the jelly-roll method may be significantly improved by replacing opaque zones with transparent phase-shifting ones. This raises the highest

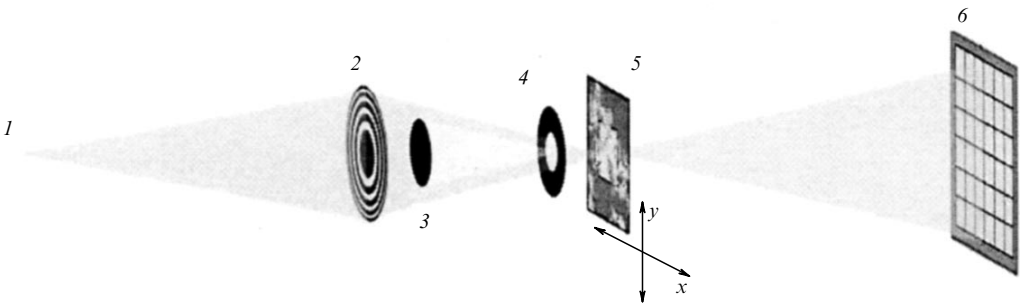

Figure 4. Optical configuration of an SFXRM: *1* — radiation source, *2* — objective FZP, *3* — stop, *4* — order-sorting aperture, *5* — raster-scanned sample, and *6* — detector.

theoretical FZP efficiency from 10% to 40% for hard X-rays, for which the loss due to absorption is lower [64]. For instance, Koyama et al. [67] were able to achieve a first-order focusing efficiency of 27% for an FZP composed of $Si/MoSi_2$ layers with an outer zone width of 40.4 nm, a zone plate thickness of 32 μm, and an aspect ratio of 792 in an operation with 20-keV X-rays.

3.2 Condenser optics

The purpose of condenser optics consists in collecting and delivering to a sample as many photons as possible, so as to shorten the information acquisition time required for image construction. All TXMs that employ an FZP as an objective lens necessitate a condenser to illuminate the object field with a hollow cone of X-rays. This kind of illumination, as a rule, may be achieved with a stop placed in the central part of the condenser FZP. This prevents object illumination by the zero diffraction order of the FZP.

The condenser must comply with requirements pertaining to the angular divergence of a beam directed to a sample to obtain the optimal image quality. The sample illumination may be characterized as a matching parameter, which is defined as the ratio between the condenser (NA_c) and objective (NA_o) numerical apertures: $\sigma = NA_c/NA_o$. Perfect matching corresponds to $\sigma = 0$, its complete absence corresponds to $\sigma \geqslant 1$, and for $0 < \sigma < 1$ we are dealing with partial matching [3, 53, 68]. The resolution is often represented in the form of the ratio $k_1\lambda/NA_o$, which is equal to $2k_1\delta r_N$ for the first diffraction order, according to formula (5). The value of k_1 is determined by σ and the magnitude of aberrations. Theoretically, k_1 decreases from 0.5 in a matched system to 0.28 in an unmatched system with $\sigma = 1$ [52]. The authors of Ref. [69] arrived at the conclusion that, from the standpoint of maximizing spatial resolution, the σ magnitude must fall in the range from 0.4 to 0.7. Therefore, for a partial matching, the spatial resolution may be better (smaller) than the outer zone width of an FZP [52].

The function of a condenser is traditionally fulfilled by a large-diameter FZP (on the order of 10 mm or more) with several dozen thousand zones [70], since the FZP should collect as large a fraction of the radiation delivered by the X-ray source as possible. For instance, described in Ref. [52] is a condenser FZP with $\delta r_N = 60$ nm, $N = 41{,}700$, $D = 10$ mm, and a central stop 5 mm in diameter, while the objective FZP parameters were $\delta r_N = 25$ nm, $N = 300$, and $D = 30$ μm.

Since the zone plates refer to diffraction optical elements, they are not free from chromatic aberrations, and the image quality depends heavily on the monochromaticity of image-forming radiation. To provide the requisite monochromaticity (recall that the objective must be illuminated by X-rays with $\Delta\lambda/\lambda \leqslant (mN)^{-1}$), an aperture stop of small size c is placed immediately near the sample (Fig. 5). This aperture stop, together with the condenser FZP, operates as a linear monochromator. In this case, the transmission spectral band is expressed by the formula $\Delta\lambda/\lambda = 2c/D$ [71].

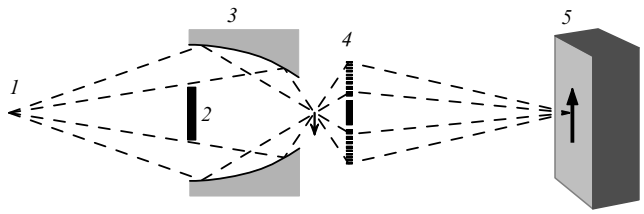

Figure 6. Schematic of a TXM with an ellipsoidal capillary as condenser: *1* — radiation source, *2* — stop, *3* — capillary, *4* — objective FZP, and *5* — detector [73].

Recent years have seen the development of alternative type condensers, in particular those based on monolithic hollow glass capillaries (Fig. 6). Such condensers are employed with different X-ray sources: SR sources [72–74], microfocus tubes [75], and laser plasma sources [30, 76]. X-rays are reflected from the inner surface of a hollow capillary, which is ellipsoidal or parabolic in shape. These optical elements are achromatic and, consequently, they do not function like monochromators, as with FZPs [77]. Their numerical aperture is limited only by the critical angle of total external reflection for X-rays. These capillaries provide a uniform illumination of a sample by a hollow cone of X-rays and form a focal spot approximately 1 μm in size [73].

Capillary condensers offer several advantages over FZP condensers [3]: (1) they are more readily available; (2) they permit varying the energy with a monochromator without the necessity of replacing the condenser when the X-ray energy is varied; (3) their NA may correspond to the NA of any objective FZP; (4) their efficiency is 3–15 times the FZP efficiency in the absence of unwanted high diffraction orders; (5) they are more reliable and durable; (6) they are resistant to heat load and mechanical damage, and (7) they do not require placing a stop near the focus to form the requisite transmission bands and therefore do not limit the size of the sample holder or the capability of controling it.

In the operation with the laser plasma sources, for a condenser use is often made of a normal-incidence multilayer mirror [78–80]. Such a mirror combines the functions of a

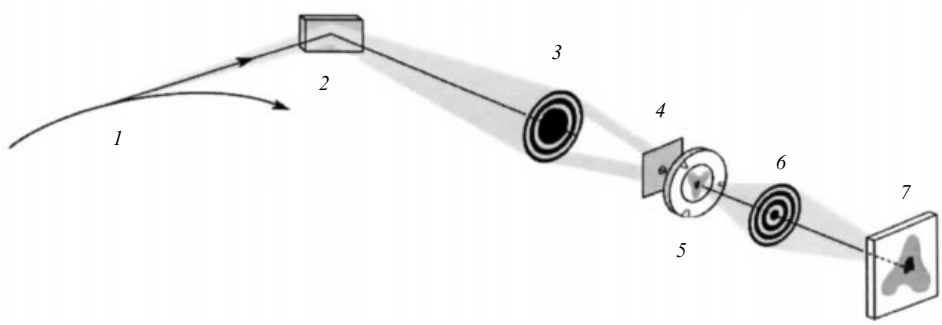

Figure 5. Schematic of a TXM operating on the bending magnet of a synchrotron storage ring [52]: *1* — trajectory of the electrons generating SR, *2* — mirror, *3* — condenser FZP with a central stop, *4* — aperture serving to form an X-ray beam with the desired relative spectrum width, *5* — sample holder, *6* — objective FZP, and *7* — detector.

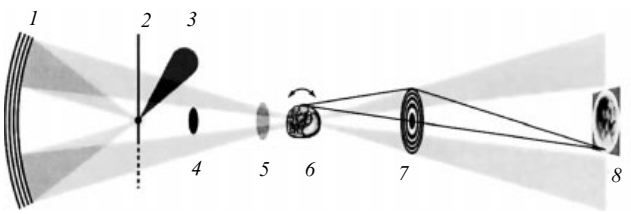

Figure 7. Schematic of a compact laboratory TXM: *1* — normal-incidence mirror, *2* — liquid jet target, *3* — laser pulse, *4* — central stop, *5* — filter rejecting the scattered laser radiation, *6* — sample, *7* — objective FZP, and *8* — detector [79].

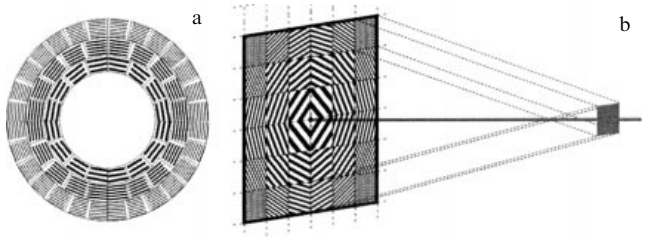

Figure 9. Sectoral grating condensers of round [82] (a) and square [84] (b) shapes.

monochromator and a condenser, focuses X-rays on the sample (Fig. 7), and offers several advantages, including a high efficiency, a clearly defined spectral selectivity, a large numerical aperture, and simplicity of alignment.

For a hard X-ray condenser, the authors of Ref. [81] proposed a cylindrical X-ray prismatic lens adapted to the numerical aperture of the image-forming objective lens. The cylindrical lens consists of a large number of layers containing a multitude of optical elements in the form of prisms (Fig. 8). The prisms change the direction of the primary parallel X-ray beam. With the use of such a prism it was possible to illuminate a field of view of 80×80 μm^2 at a focusing efficiency of 88%.

X-ray optical elements (FZPs, capillaries, mirrors) focus beams on a spot whose dimension is, as a rule, smaller than the microscope field of view. As a result, the X-ray optical elements cannot provide a uniform illumination of this domain. A new condenser, which offers certain advantages over other condenser systems, was developed on the basis of the diffraction optics in Ref. [82] and then tested in Ref. [83]. Its design is underlain by the idea of dividing an ordinary FZP into sectors and retaining the local period constant within each sector (Fig. 9a). As a result, each sector will provide a uniform illumination in the focal plane. The overlapping of the X-rays from different gratings results in a significant lowering of the spatial coherence in the sample plane, so no quality-impairing diffraction pattern (speckle noise) forms on the sample image, which permits using the condenser in a high-intensity beam. However, the superposition of radially asymmetrically distributed patterns makes up an approximately round illuminated domain with considerable 'tails'. The sectorial condenser structure shown in Fig. 9b permits eliminating the 'tails' and augmenting the intensity of the uniformly illuminated domain. Another advantage of employing a square field of view is that the active detector area is, as a rule, a square. In this case, the illumination by the beam formed with the condenser may be perfectly matched to the detector size [84].

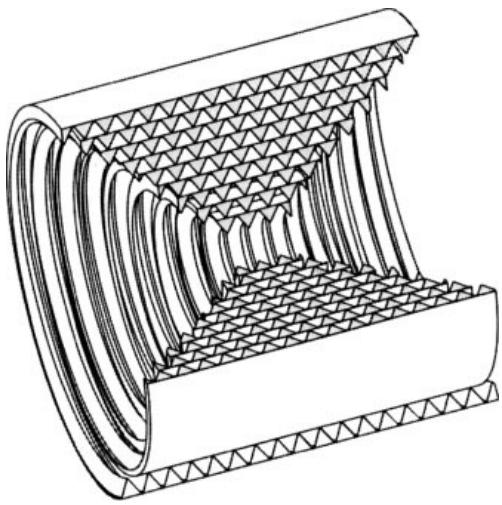

Figure 8. Schematic representation of a cylindrical prismatic X-ray lens [81].

4. Two-dimensional imaging with the use of amplitude contrast

When the intensity of a beam incident on a substance layer of thickness t is I_0, according to the Bouguer–Lambert–Beer law the beam intensity at the output of the layer is expressed as $I = I_0 \exp(-\mu t) = I_0 \exp(-\tau_m \rho t)$, where μ and τ_m are the linear and mass absorption coefficients, respectively, and ρ is the substance density. The absorption coefficient depends largely on the wavelength and the atomic number Z: τ_m increases rapidly according to the relation $\tau_m \sim Z^3 \lambda^3$.

The X-ray amplitude (absorption) contrast is related to the density and/or thickness variations of the neighboring regions of an object under investigation and permits studying its morphology and the special features of its internal structure. This contrast was employed for studying biological objects, which is reflected in several reviews concerned with the biological applications of X-ray microscopes [3, 38, 85]. Emphasis was placed on the high-resolution imaging of separate cells in the 'water window' ($\lambda = 23-45$ Å), including in the investigations of human spermatozoids [86], malaria parasites in red corpuscles [87], protozoa [88], and chromosomes [89]. Figure 10 depicts the images of neurons [90], a human spermatozoid [86], and diatoms [81], which were obtained with a TXM.

Many investigations of soft materials and biological samples are limited by the level of radiation damage rather than the microscope efficiency. Low-temperature (100 K or below) sample measurements are known to preserve morphology, limit the mass loss, and permit suppressing the radiolysis in hydrated samples. Investigations with the aid of a cryogenic module for fast frozen cells not subjected to the action of chemical fixatives or contrast-increasing agents bear the strongest resemblance to the investigations of cells in their natural state.

The past three decades have seen the development of soft X-ray microscopy techniques intended for visualizing materials and biological objects with a resolution of several dozen nanometers. By contrast, several hard X-ray microscopy techniques with comparable spatial resolution capable of lending impetus to nano- and mesoscale materials science

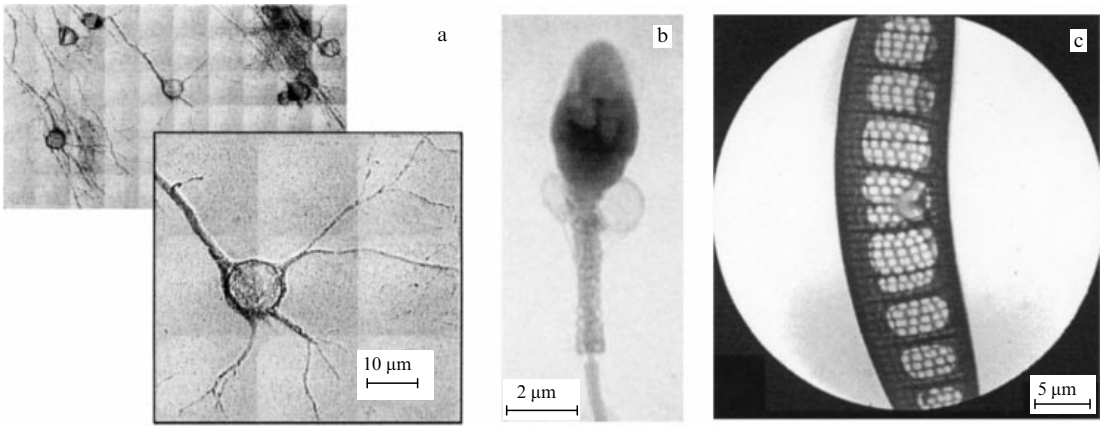

Figure 10. (a) Image of mouse neurons (the inset to the lower right part of the figure is an enlargement [90]). (b) Image of a human spermatozoid. It was possible to visualize the image details in the basal plate region only with the aid of a TXM and not with a light microscope [86]. (c) *Diatomeae* image [81].

research [91] made their appearance much later. In recent years, they have been employed to investigate colloids [92, 93], modern integrated circuits [94], and power cells [95, 96].

5. Two-dimensional imaging with the use of phase contrast

In the passage through a substance, an X-ray wave not only undergoes absorption but also changes its phase. The X-ray phase shift $\Delta\Phi$ acquired in passing through a sample of thickness t depends on the decrement of X-ray refractive index δ:

$$\Delta\Phi = \frac{2\pi}{\lambda}\,\delta t\,, \tag{10}$$

where $\delta = 1 - n = \rho\lambda^2 r_0 N_A Z/(2\pi A)$ [97] (n is the X-ray refractive index, N_A is the Avogadro constant, r_0 is the classical electron radius, and A is the atomic weight of the sample material). Imaging in the phase contrast mode is quite often the mode of choice due to the possibility of achieving a higher contrast ratio, especially for higher X-ray energies. For soft tissues with different densities, the differences in X-ray phase shift are much greater than those in linear absorption coefficients. A phase contrast imaging may therefore improve the sensitivity of X-rays to small structural variations of the objects under investigation. The method is highly efficient for characterizing weakly absorbing (phase) objects with small variations of the absorption coefficient inside of them: the method relies on variations of the refractive index decrement δ in the object.

The object being examined may deflect X-rays from the initial trajectory by an angle θ. The angle θ is proportional to the local gradient $\partial\Phi/\partial x$ of the object phase variation and may be defined as $\theta = (\lambda/2\pi)(\partial\Phi/\partial x) = (\partial\delta/\partial x)\,t$ (x is the axis perpendicular to the optical axis of the microscope). In the case of a flat interface between media with refractive indices n_1 and n_2, X-rays incident at an angle θ_i will deflect from the initial direction, according to Snell's law, by an angle $\theta \approx (n_1 - n_2)\,\mathrm{tg}\theta_i$. For a curved interface, the angle θ_i varies smoothly, resulting in X-ray divergence (convergence) at the output from the sample.

5.1 Zernike phase contrast

One way to obtain a phase contrast passes through the exploitation of the Zernike method [98]. To provide the Zernike phase contrast, a hollow cone of sample-illuminating X-rays is oriented toward a narrow ring in the rear focal plane of an FZP (Fig. 11). The phase ring thickness is selected so as to change the phase of the X-rays undeflected by the sample through $\pm\pi/2$. On the other hand, X-rays may be deflected by the sample (diffract from it) and reach the detector bypassing the phase ring. As a result, the interference between the two types of optical signals produces in the detector the image of phase variations in the sample [3, 5, 31, 38].

The Zernike X-ray phase contrast was first demonstrated in Ref. [99] with the use of soft X-rays, and in Ref. [100] for hard radiation impact. This contrast turned out to be highly efficient in the observation of small variations of electron density in biological samples [101–103] (Fig. 12), medical examinations [34, 50, 104], studies of fuel cells [105], and integrated circuits [100, 106].

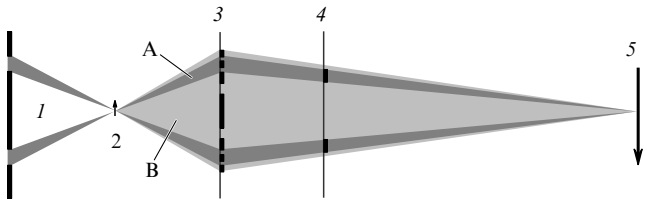

Figure 11. Schematic representation of a TXM operating in the Zernike phase contrast mode: *1* — hollow conical X-ray beam formed by a condenser, *2* — sample, *3* — objective FZP, *4* — phase ring, *5* — detection plane; A — nondiffracted radiation, and B — diffracted radiation [31].

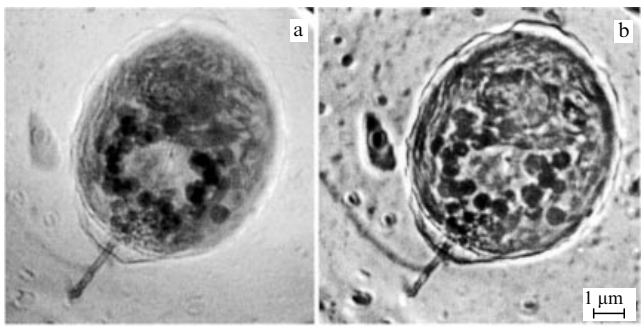

Figure 12. X-ray image of a *Chlamydomonas rheinhardtii* alga ($\lambda = 2.4$ nm): (a) amplitude, and (b) phase contrast images [101].

For soft X-ray radiation, materials usually exhibit a higher absorption for a given value of the phase shift, and so the design of phase rings should be a trade-off between the magnitude of the phase shift and the beam attenuation. One way to reach this trade-off is to incorporate the $\pm\pi/2$ phase shift directly into the objective FZP, which transforms it into a Zernike FZP. Both positive ($+\pi/2$) and negative ($-\pi/2$) Zernike phase contrasts may be realized. The transformation of an ordinary FZP into the Zernike FZP involves the introduction of a phase filter with the shape and area corresponding to the nondiffracted radiation employed in imaging [107].

However, it is pertinent to note that the Zernike X-ray phase contrast may produce halo effects which affect the analysis of sample morphology [5, 108].

5.2 Differential interference phase contrast

For differential interference contrast (Nomarsky contrast), two wavefronts slightly inclined to each other are formed with either a double FZP or a beam splitter placed in front of an FZP. In the former case, the first FZP (ZP1 in Fig. 13) splits the incident plane wave into a zero-order (transmitted) plane wave and a set of spherical waves of the first and higher orders. The second FZP (ZP2), which is shifted relative to the first one in the sample plane, interacts with the radiation emanating from ZP1. Only the combinations of the zero order of ZP1 with the first diffraction order of ZP2, and vice versa, will make efficient contributions to the image formation.

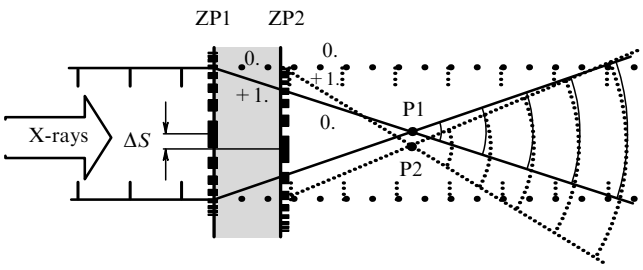

Figure 13. Formation of differential interference contrast with a twin FZP [109].

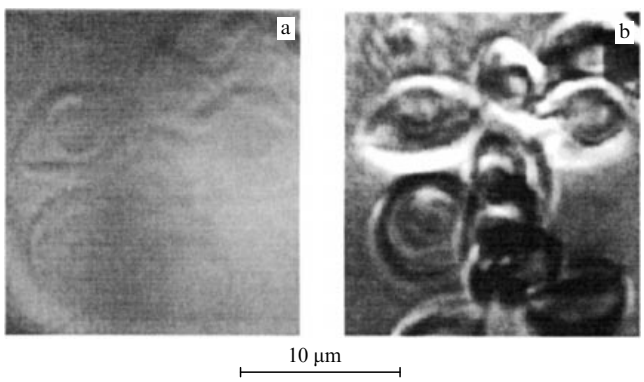

Figure 14. X-ray images of the giant spores of *Dawsonia superba* moss obtained with (a) absorption and (b) differential interference contrasts [109].

A necessary condition for attaining differential interference contrast is a sufficiently high degree of coherence in the sample plane: the shift ΔS in the sample plane must not exceed the transverse coherence length. In the detector plane, the interference of two spherical waves emanating from foci P1 and P2 will produce an interference pattern with fringes spaced at $\Delta y = \lambda z_0/\Delta S$ (z_0 is the distance of the rear FZP focal planes from the detector). ZP1 and ZP2 have equal focal lengths, and their spacing along the optical axis must be small in comparison with their distance from the image plane. The image may be observed in differential interference contrast for $\Delta S < d$ (d is the spatial resolution) [109, 110].

The interference pattern is aligned to be centered on a bright fringe and shifts in the interference fringe are proportional to the local phase gradient of the sample [111]. Phase objects undetectable with ordinary absorption contrast microscopy become visible due to interference (Fig. 14).

The main advantages of the differential interference contrast method are: (1) it allows invariance of the detector and source arrangement geometries and therefore may be used in STXM and TXM modes; (2) it is not really dependent on the X-ray beam coherence due to a small wavefront shift and a short difference in optical path lengths, and (3) it easily conforms to the spatial limitations imposed by the very short focal FZP length, when using the soft X-rays [5].

The idea of exploiting a single-element FZP for phase contrast optics was first conceived by Chang et al. [112]. Two types of 'twin' FZPs have been demonstrated to date: an XOR FZP obtained by combining (by way of imposition) a two-dimensional grating and an FZP with the help of a logical operation XOR (usually used to decrease the displacement of bits produced by a hardware random number generator) [113, 114] (Fig. 15a), and a twin FZP [115] (ZPD in Fig. 15b). The properties of differential interference microscopy are characterized by two parameters: the lateral displacement, and the phase shift. For an XOR FZP, the lateral displacement is determined by the FZP diameter, the width of its outer zone, and the grating period P: $\Delta x \approx 2\delta r_N D/P$; the phase shift $\Delta\Phi$ depends on the relative position of the grating and the FZP: $\Delta\Phi = 2\pi(\Delta a/P)$, where Δa is the displacement of the grating

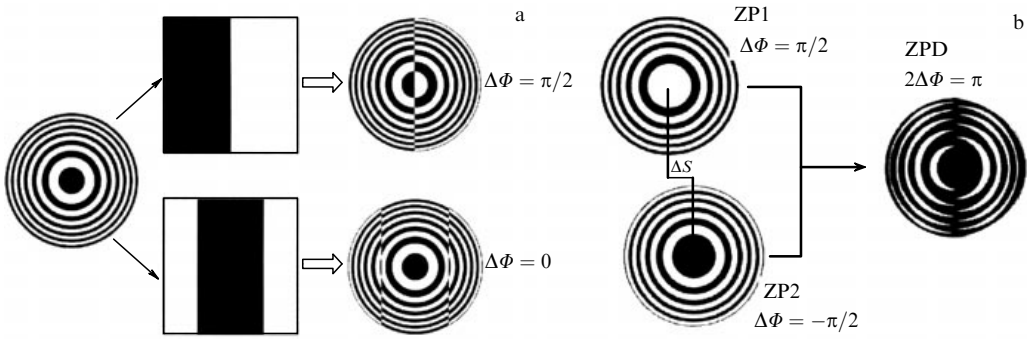

Figure 15. FZP transformation into an XOR FZP [113] (a) and a twin FZP [115] (b).

relative to its zero position. The phase shift $\Delta\Phi = \pi/2$ corresponds to the grating displacement by a quarter of a period ($\Delta a = P/4$) from its zero position (Fig. 15a).

5.3 Differential phase contrast

In the raster scanning in an STXM, the detector usually measures the total X-ray radiation intensity to give an incoherent bright-field image (absorption contrast). Phase contrast has historically been less used in STXMs. Nevertheless, the effects of X-ray refraction and diffraction by the sample lead to signal redistribution over the detector, which may be transformed into a phase contrast imaging. Since the detector response function may be positive as well negative, in the STXM it is possible to realize several new imaging modes which have no practical equivalents in TXMs. It is precisely this that led to the idea of the differential phase contrast method [116–118].

The differential phase contrast method requires the employment of a detector with an antisymmetric response function which is sensitive to any intensity redistribution in the detector plane, so that different linear combinations of segmented detector signals permit simultaneously recording of the absorption contrast and the phase contrast image. The advantage of applying this detector is that the detector response functions may be modelled after the image formation by combining the corresponding signals from different segments. This signifies that different combinations of detector segments may be simultaneously employed and that one sample scan provides a sufficient amount of data for analyzing both the amplitude and phase of the transmitted radiation: difference images between opposite segments determine the differential phase contrast, while the sum of all signals determines the absorption contrast of the image.

Diode segmented detectors [118–121] have been widely adopted in the investigation of biological objects [118, 122]. Figure 16a demonstrates the exterior view of a detector containing seven segments: segments 1–3, which record the light cone emanating from the object under investigation, are intended for obtaining bright-field amplitude contrast [119], while segments 4–7 may be employed to obtain dark field images [116, 123, 124] and measure differential phase contrast. Figures 16b and 16c demonstrate the advantage of differential contrast (the image is formed by the difference between the X-ray intensities recorded by segments 4, 5 and 6, 7) over the amplitude contrast (all the segments were exposed to X-rays) [118].

Among the disadvantages of diode segmented detectors is the necessity of selecting the detector configuration at its design stage, as well as the existence of a clearly defined central axis which must coincide with the microscope's optical axis. Optimal design flexibility may supposedly be reached with the use of an entirely pixeled detector like a CCD, whose response function may be arbitrarily changed after data acquisition and the effective reaction of every pixel is specified by a computer [125–128].

However, phase contrast images are sometimes hard to interpret due to the differential nature of the signal and its directional dependence. In the view of the authors of Ref. [129], there are two quantitative image reconstruction methods [130, 131]. The first method [130] defines the corresponding contrast transfer function in the detector sectors and inverts this function to determine the X-ray phase shift and absorption in the sample. This method is the most general and may be applied to any configuration of the detector segments. The method proposed in Ref. [131] expands the sample's transfer function in a Taylor series and demonstrates that the main influence of the sample on the intensity distribution in the detector plane reduces to the intensity attenuation in accordance with the average X-ray optical path in the sample, and that the deflection of X-rays is proportional to the local gradient of the refractive index in the sample.

6. X-ray spectromicroscopy

The absorption of X-ray radiation by a substance is due to the interaction of photons with inner-shell atomic electrons. When the photon energy exceeds the electron binding energy (the excitation threshold), an electron may be removed from the atom, which gives rise to an abrupt increase (jump) in X-ray absorption (Fig. 17a). The wavelength corresponding to the excitation threshold energy is termed the absorption edge of a given element. The absorption edge is a characteristic quantity of each chemical element, which makes it possible to unambiguously identify the chemical element from its position on the absolute energy scale.

The spectroscopy energy range in the domain of an X-ray absorption edge is divided into two parts:

(1) a low-energy domain, in which multiple photoelectron scattering is significant. This domain is termed the X-ray absorption near edge structure (XANES) or near edge X-ray absorption fine structure (NEXAFS);

(2) a high-energy domain, referred to as the extended X-ray absorption fine structure (EXAFS), in which the main contribution to the absorption is made by a single photoelectron scattering.

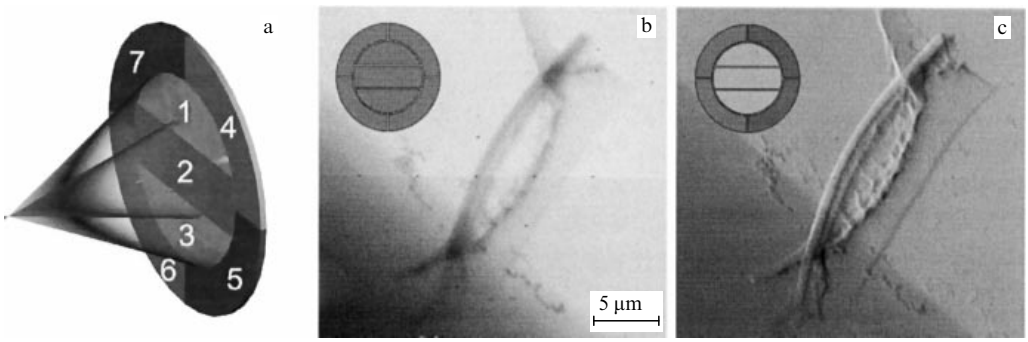

Figure 16. (a) Detector with seven active segments [119]. Absorption (b) and phase (c) contrast images of a phytoplankton cell ($E = 1.79$ keV) [118] (see explanation in the text).

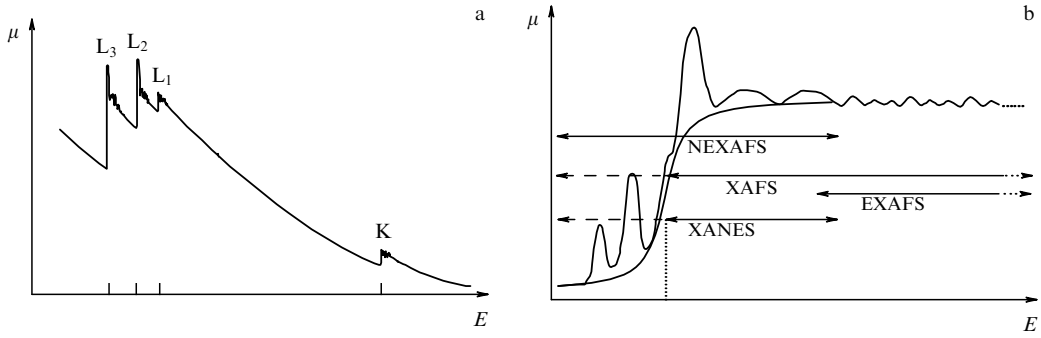

Figure 17. Schematic representation of the X-ray absorption coefficient as a function of the X-ray primary beam energy (a) for four X-ray absorption edges (K, L_1, L_2, and L_3) [132], and (b) in the region of an absorption edge [10].

As a rule, the NEXAFS spectral domain ranges from an energy of ≈ 10 eV lower to an energy of ≈ 40 eV higher than the absorption edge (Fig. 17b). XANES is often assigned to the same domain as NEXAFS, but sometimes the domain preceding the absorption edge is excluded. Encountered in the literature are some 'semantic' differences in the usage of the terms NEXAFS and XANES. The differences pertain to the energy range employed in experiments: the term XANES is used more often in experiments with hard X-rays, and the term NEXAFS in soft X-ray experiments. In what follows, we will employ only the term NEXAFS to avoid confusion.

In the NEXAFS mode, a considerably larger number of surrounding atoms are involved in the scattering than in the EXAFS mode, with the atoms participating in the scattering not only from the first coordination sphere but also from the spheres located at a distance well away from the absorbing atom. An analysis of NEXAFS spectra permits gaining information about the local geometry of the arrangement of atoms near the absorbing atom, including valence-bond angles, which have only a slight effect on the EXAFS spectrum [10, 132–134].

6.1 Chemical mapping

A high energy resolution ($E/\Delta E > 200$) is required for soft X-ray NEXAFS microscopy with a high spectral sensitivity. It is most easily achieved with a crystal monochromator or a diffraction grating placed in front of a microscope. An STXM usually provides a resolving power of 2000–5000. Condensers employed in TXMs offer a relatively low energy resolution (about 0.8 eV), which limits the employment of TXMs for spectromicroscopy [134].

The distribution of a specific element may be reconstructed by comparing two images obtained at energies above and below the corresponding absorption edge [135, 136] (Fig. 18). This method applies to samples containing chemical elements whose absorption edges do not overlap. The situation changes when the sample is composed of a mixture whose main constituent is the same element. For instance, an STXM was employed in Ref. [137] to study the mixture of a styrene–acrylonitrile copolymer (SAN) and poly-isocyanate-polyol with poly-additions (PIPA). The chemical image selectivity at the K absorption edge of carbon furnishes an unambiguous identification of SAN and PIPA particles. Since the spectra of both SAN and PIPA exhibit a strong absorption at $E = 285.0$ eV (Fig. 19a), particles of both types are seen in images obtained at $E = 285.0$ eV (Fig. 19b). For $E = 286.7$ eV, strong absorption is exhibited only by the SAN particles (Fig. 19c). Upon subtraction of the image in Fig. 19c from the image in Fig. 19b, the PIPA particles are readily identifiable (Fig. 19d).

An STXM may be used for a quantitative elemental analysis with a submicrometer resolution if the reference NEXAFS spectra were obtained on an accurate mass absorption coefficient scale. The quantitative composition may be mapped with the help of, for instance, singular value decomposition analysis of X-ray microscopy images [138]. Singular value decomposition calls for *a priori* information about the sample and it is applicable only when the sample's composition is known. Furthermore, the linear absorption coefficients of the components should be precisely known, so as to minimize systematic errors in the analysis. Every image

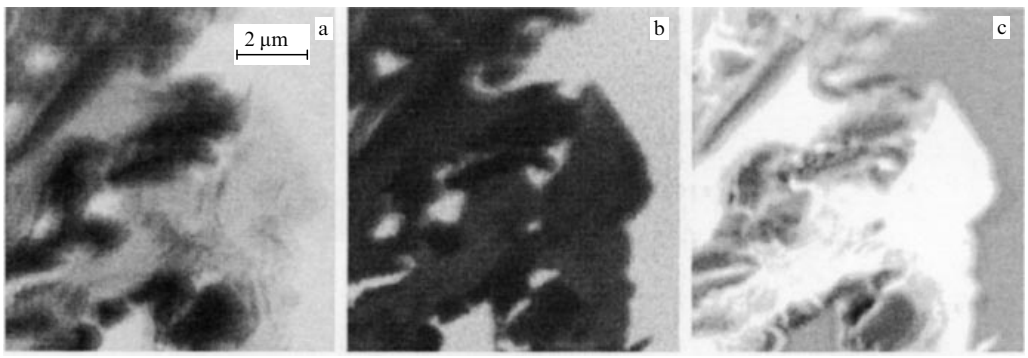

Figure 18. Maps of carbon distribution in a thin slice of upper soil layer from the Arnot Forest in the north of New York State. Images corresponding to an energy (a) below ($E = 280$ eV) and (b) above ($E = 310$ eV) the K absorption edge of carbon. (c) Image obtained by subtraction of the image in figure (a) from the image in figure (b). Bright domains in figure (c) correspond to a high carbon concentration [135].

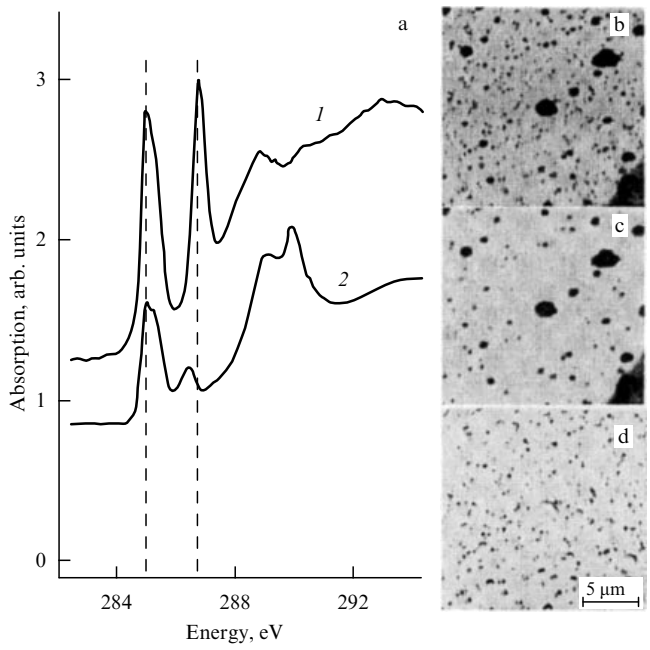

Figure 19. (a) NEXAFS spectra of polyurethane containing SAN (curve *1*) and PIPA (curve *2*) particles. Images obtained at $E = 285.1$ eV (b) and 287.2 eV (c). (d) Image obtained by subtracting the image in figure (c) from the image in figure (b) — only PIPA particles are seen. The darker color in figures (b–d) corresponds to a stronger X-ray absorption [137].

is transformed into the optical density (OD): $\mathrm{OD} = -\ln(I/I_0) = \tau_m \rho t$, where I is the transmitted radiation intensity, and I_0 is the intensity of the primary X-ray beam. Combining X-ray absorption images obtained at two or more energies (for which there is a difference in X-ray material absorption) results in a system of linear equations which may be solved if the number of images is greater than or equal to the number of components. Therefore, the array of approximation coefficients for a given component obtained by comparing (fitting) individual spectra with the linear combination of the reference spectra leads to a quantitative chemical mapping of the component [139, 140].

For typical features 200 nm or below in size, the acquisition of high-quality spectra becomes complicated: there should be no lateral beam displacement on a sample in the alignment of focusing. These limitations complicate the recording of spectra from domains smaller than ≈ 200 nm in width, while soft X-ray microscopes range from 30 to 50 nm in resolution. The authors of Ref. [141] came up with the approach of forming a 'stack' of images from a small domain, obtained by varying the X-ray energy by a small increment.

When the optical density is measured in the set of discrete energies E_n, $n = 1, \ldots, N$ for a mixture of $s = 1, \ldots, S$ different components of thickness t_s with the use of heterogeneous sample columns $p = 1, \ldots, P$, the measurement of the optical density OD_{np} for a single X-ray photon energy n in one column p is given by the formula

$$\mathrm{OD}_{np} = \mu_{n1} t_{1p} + \mu_{n2} t_{2p} + \ldots + \mu_{nS}\, t_{Sp}\,. \tag{11}$$

Because of the departures from the perfectly rectilinear motion of the sample holder used to compensate for the zone plate position variations upon the X-ray photon energy variation (and, therefore, focal length variations), these images are aligned using the aXis2000 code package [142] and the subsequent formation of a data matrix $\mathrm{OD}_{N\times P} = \mu_{N\times S} t_{S\times P}$ [3, 143]. When the exact μ_{Ns} values in the absorption spectrum for each sth component of the sample are known, it is possible to find the spatially allowed component thicknesses $t_{S\times P}$ in the matrix inversion:

$$t_{S\times P} = \mu_{S\times N}^{-1}\, \mathrm{OD}_{N\times P}\,. \tag{12}$$

The spectra matrix $\mu_{N\times S}$ with all known components may be inverted using singular value decomposition analysis [138]. Since the 'stack' method permits obtaining images at short energy intervals, it is possible to observe fine spectral features.

In many areas of research like biology or environmental science, the complexity of sample composition and the possibility of reactions among its components have the consequence that all absorption spectra $\mu_{N\times S}$ of the elements present in the sample cannot be known beforehand. In this case, an approach is possible which initially leans upon the main component analysis [143] to orthogonalize and diminish the noise of $\mathrm{OD}_{N\times P}$ matrix components and then performs cluster analysis to collect (make up) a set of columns proceeding from the similarity of the characteristic spectral features [144]. This method gives rise to a set of absorption spectra $\mu_{N\times S}$, where S is now the index of the spectra obtained from experimental data. An advantage of this approach is the emerging ability to improve the signal/noise ratio for the spectra of heterogeneous samples [3].

The broad possibilities of chemical mapping for the study (qualitative and quantitative) of condensed media are attested to by a wealth of publications concerned with biomedicine and biomaterials [10, 38, 140, 145–155], synthetic polymers and biopolymers [19, 137–139, 142, 156–172], gels [173–175], carbon nanomaterials [176–179], charging devices and fuel cells [16, 180–184], fuels [185, 186], the environment [10, 23, 135, 172, 187–189], and botany [190–194].

6.2 Valence determination

It is common knowledge that the position of an X-ray absorption edge greatly depends on the degree of oxidation of the absorbing atom: with increasing degree of oxidation, it shifts to the higher energy side. For instance, the position of the K absorption edge of Se changes with an increase in oxidation degree (the oxidation degrees Se(+VI), Se(+IV), Se(0), and Se(−II) correspond to energies of 12.665, 12.662, 12.658, and 12.656 keV) and is therefore a characteristic of the Se oxidation state [195]. A comparison of the measured spectrum of a sample with that of a compound containing an absorbing atom with the known valence allows the researcher to make an inference about the charge state of this atom in the sample under investigation [6, 196–201].

Thus, the authors of Ref. [196] studied the biomineralization of the bacterium *Acidovorax sp.* BoFeN1 in the presence of dissolved Fe(II). Taking advantage of the difference between the NEXAFS spectra of the Fe(III) and Fe(II) phases, they discovered that oxidation started in the periplasm with the subsequent formation of Fe(III) minerals on the cell's surface. The process eventually results in complete decoration of the cell by Fe(III) minerals. In Ref. [197], a TXM was employed to trace valence variations in thin-film resistive switching $SrTiO_3$ devices. Several real-time investigations were made: the L_2 and L_3 absorption edges of iron were employed to monitor *in situ* valence and the coordination of iron-bearing formations, whereas the K absorption edge of oxygen was exploited to separate different oxygen-

bearing formations in the Fischer–Tropsch catalyst [198]. Using a TXM, an *in operando* study was made of the nonuniformities in the phase distribution of $LiFePO_4$ multiparticles which participate in the lithium depletion of electric batteries [199].

6.3 Investigation of magnetic structures

Unlike the X-ray radiation of laboratory sources, SR is highly polarized. The polarization is linear in the orbit plane. In this case, the electric intensity vector is perpendicular to the direction of SR propagation and lies in the orbit plane, while the magnetic vector is perpendicular to this plane. The radiation outside of the orbit plane is elliptically polarized, the radiation being left-polarized on one side of the plane and right-polarized on the other side. In general, the polarized radiation is composed of linearly and circularly polarized waves. The polarization depends on the wavelength and the angle of deflection from the tangent to the orbit. The polarization may turn out to be an important property in the investigation of anisotropic or polarized objects. In this case, varying the direction of the electric vector or the degree of beam polarization may yield information unobtainable with the use of other X-ray radiation sources [202, 203].

It is well known [20, 21, 204, 205] that the combination of a high-resolution X-ray microscope and the effect of X-ray magnetic circular dichroism (XMCD), i.e., with the dependence of circularly polarized X-ray absorption on the magnetic properties of a sample, provides a high image contrast of magnetic domain structures and permits obtaining information about the local spin and orbital momenta of absorbing objects. The intensity difference in the parallel and antiparallel spin orientations and magnetization directions near the L_3 and L_2 absorption edges is in quantitative agreement with the spin and orbital magnetic moment magnitudes, as well as with spin density anisotropy and orbital moment anisotropy. That is why magnetic spectroscopy is capable of determining the magnitudes, directions, and anisotropy (the directional distribution of the magnitude) of atomic magnetic moments [203]. This furnishes a unique possibility to gain information about the atomic-level structure of materials by comparing the spectra corresponding to the two X-ray absorption edges [205–207].

Images of a Cr(3 nm)/Fe(50 nm)/Cr(6 nm) multilayer system obtained at the L_3 and L_2 absorption edges of Fe are given in Fig. 20. The observed contrast change is unambiguous proof of its magnetic nature [208].

The main advantage of X-ray microscopy–XMCD symbiosis is the possibility of recording images in different external magnetic fields, which yields information about the evolution of domain magnetization throughout the full hysteresis loop [209–212]. Magnetic TXM has also been employed to study layered magnetic structures [22] and to directly observe the motion and depinning of magnetic domain walls [213–216].

Due to the temporal structure with a pulse duration of 100 ps or shorter inherent in SR, it is possible to investigate the spin dynamics [217–224]. The stroboscopic pump–probe method [22, 218] was applied for observations on a picosecond time scale, after excitation of the ground state of a vortex structure by a 1-ns long pulse generated in an external field [217]. Time-resolved soft X-ray transmission microscopy was employed to visualize the dynamics of a magnetic vortex in permalloy disks ($Fe_{19}Ni_{81}$ [218] and $Fe_{20}Ni_{80}$ [219]) with a spatial resolution of 25 nm and a temporal resolution of 70 ps. The authors of Ref. [220] observed the motion of a magnetic vortex core in a hexagonal permalloy structure.

6.4 Exploitation of orientational sensitivity

Having a long mean free path, a generated photoelectron may experience multiple scattering by surrounding atoms. That is why the shape of the NEXAFS spectrum depends not only on the bond lengths but also on the angles and symmetry of the bonds. In antimagnetic systems, linear X-ray dichroism testifies to charge asymmetry caused by the atom's environment of symmetry lower than the cubic one. In magnetic systems, polarization dependence may take place even in the environment exhibiting cubic symmetry [225]. To the degree the absorption coefficient of a specific sample's domain depends on its orientation relative to the polarization plane, the NEXAFS spectrum will vary with the variation of the orientation of the domain relative to the electric vector (Fig. 21).

X-ray microscopy and linear dichroism were first employed to show that images obtained for a fixed photon energy are orientation-sensitive [226]. The on-axis radiation of an undulator with a transverse magnetic field is linearly polarized. Thus, the utilization of STXM images obtained for two mutually orthogonal radiation polarizations permits separating out the contribution from the contrast due to orientation. Subtracting one image from the other gives the contribution from only the linear dichroism of the sample

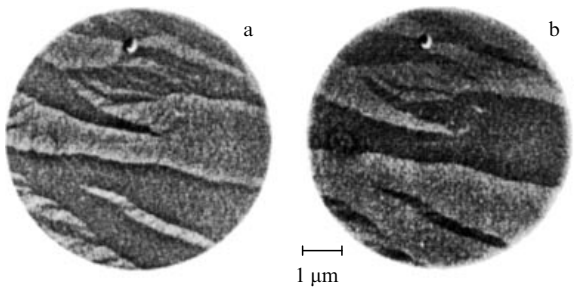

Figure 20. Images of the multilayer Cr(3 nm)/Fe(50 nm)/Cr(6 nm) film obtained at the L_3 (a) and L_2 (b) absorption edges of Fe [208].

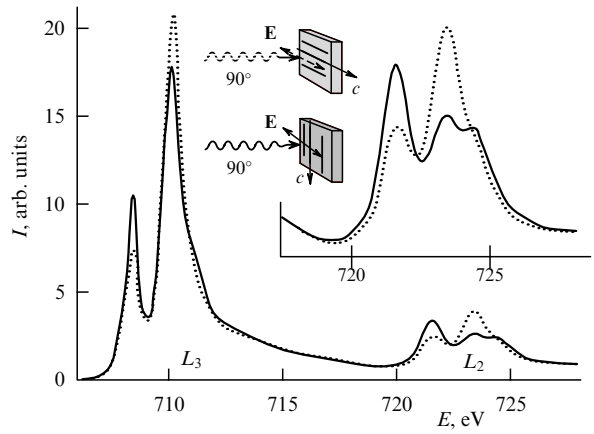

Figure 21. NEXAFS spectra of the $L_{2,3}$ absorption edges of Fe for an epitaxial $LaFeO_3$ film grown on an $SrTiO_3$ (110) substrate, which were recorded using linearly polarized X-rays. For the spectrum shown with a solid curve, the electric vector **E** is perpendicular to the crystallographic *c*-axis of the film, whereas for the spectrum depicted with a dotted curve, the vector **E** is parallel to the *c*-axis [225].

and, consequently, furnishes the mapping of object domain orientations with a good angular resolution [227].

The orientational sensitivity of NEXAFS spectra has been utilized in spectromicroscopy for investigating the orientation of molecules in organic nanomaterials [228, 229], the block structure of organic films [230, 231], organic semiconductors [232], transistors [233, 234], molecular orientation in artificial and natural fibers [226, 235, 236], as well as the structure of liquid crystals [227, 237] and carbon nanotubes [177].

7. Scanning X-ray fluorescence microscope

The principle of operation of a scanning X-ray fluorescence microscope (SXFM) is related to the photoexcitation of electrons in the sample bulk illuminated by X-rays. When the energy of the primary X-ray photon absorbed by a bound electron is higher than the binding energy of the electron, the absorbing electron will be knocked out of its atomic orbital. At the next point in time, an electron occupying a higher energy level will transit to the vacant orbital and in doing so will emit a photon of energy equal to the energy difference between the two states. The X-ray emission energy spectrum usually consists of several characteristic lines corresponding to the energy difference between the specific shell orbitals. This spectrum makes it possible to unambiguously identify a chemical element. The upside of this method is that the number of fluorescence photons is directly related to the quantity of this element in the irradiated sample volume. Therefore, by comparing the areas under the peaks in fluorescence spectra corresponding to different chemical elements, the possibility appears to determine the quantitative elemental composition of the sample [13].

The characteristic spectra may be recorded simultaneously by eight silicon drift detectors [238] (Fig. 22) or by a detector with a large sensitive area, a large acceptance solid angle, and a high count rate [239].

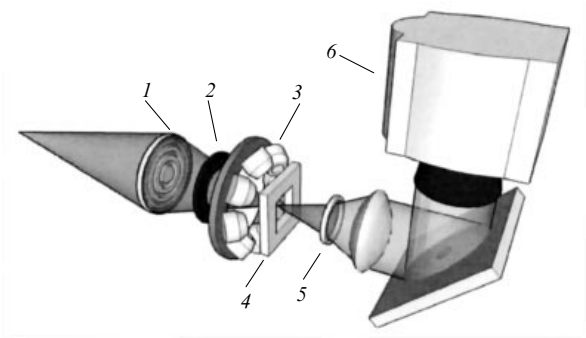

Figure 22. SXFM with a zone plate *1*, a sorting aperture *2*, a 'necklace' of energy dispersion detectors *3* of X-ray fluorescence emission, a sample holder *4*, an X-ray-to-light photon conversion system *5*, and a fast readout detector *6* [238].

The SXFM mode permits realizing simultaneously the recording of X-ray absorption (or image phase contrast) and soft X-ray fluorescence photons, which is especially attractive for biological research [240]. This mode also makes it possible to simultaneously obtain the distributions of elements with a low atomic number (from B to P) from K-series emission lines, and elements with a higher atomic number (from Ca to Nb) from L-series lines (Fig. 23).

SXFM enjoys wide application in various fields of science [240, 242]. In particular, in 2013 publications appeared dedicated to the study of intracellular cerebral metabolism of glucose [243, 244], the interactions of $CoFe_2O_4$ magnetic nanoparticles with U87MG cells [245] and digestive juices of a model invertebrate organism [246], and the asbestos–iron interaction in human pulmonary tissues [247].

8. Three-dimensional imaging (tomography)

An important advantage of X-rays is their high penetrating power, and the majority of investigations are concerned with the study of samples too thick for electron microscopes. However, for thick samples the problem of overlapping the internal structural details lying at different depths in the object under study may arise. That is why 2D images are often too complicated and inconclusive, and then three-dimensional (3D) visualization becomes particularly desirable. Three-dimensional X-ray microscopy emerged as an imaging technique capable of revealing the 3D microstructure for a broad range of materials. The nondestructive nature of X-rays made this technique particularly attractive and facilitated the acquisition of 3D information about a sample not only in a real-time mode, but also in the presence of various external actions.

X-ray tomography was first demonstrated by Haddad et al. [248] in 1994 with the use of an STXM, and three years later by Lehr [249] with the use of a TXM. Subsequently, transmission X-ray microscopy came to the forefront in tomography owing to its high data collection rate. Therefore, the implementation of commercial production of tomographic TXMs by Xradia (in 2013, Xradia became a part of Carl Zeiss Microscopy and received a new name: Carl Zeiss X-ray Microscopy Inc., Pleasanton, CA, USA) has to be regarded as one of the most important achievements in the area of X-ray microscopy; these TXMs are capable of constructing 3D images with a resolution of at least 50 nm, and a field of view up to 65 μm [33, 75, 250].

In the collection of data for tomographic reconstruction, the sample holder should ideally ensure rotation of a sample through at least 180° about the axis normal to the direction of

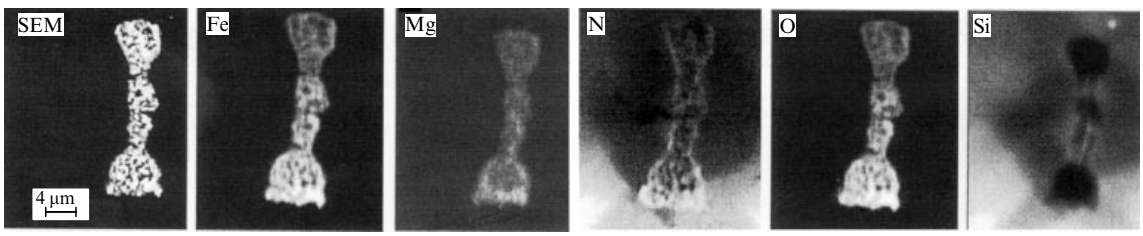

Figure 23. Images of an asbestos particle extracted from a pulmonary tissue, which were made with a scanning electron microscope (SEM) in the rays of characteristic lines of Fe, Mg, N, O, and Si at beam energies of 1.935 keV (Si, Mg) and 0.9 keV (Fe, N, O) [241].

primary X-ray beam propagation, the eventual spatial resolution improving with an increase in the number of projections. The projections obtained for different angular positions of the sample go through alignment with respect to a common rotation axis. There are several algorithms for taking this step. The IMOD code [251] is supposedly the most popular one, which makes use of reference marks for the alignment. Unlike IMOD, the Alignator code [252] searches for local regions on different angular projections which serve to align these regions, and so the need to use references for the 3D imaging reconstruction no longer stands.

The methods employed for volume image reconstruction differ primarily in the level of noise and/or the number of artifacts present in the final reconstructed object, as well as in the smoothness or sharpness of the object boundary in the image. The purpose of all these methods is to minimize the noise with retention of all necessary image details. However, the techniques that suppress noise are likely to deteriorate the resolution. The attainable tradeoff between the noise level and the resolution depends, as a rule, on the technique employed for the subsequent reconstruction [253].

The algorithm used most widely for reconstructing 3D images has come to be known as filtered back projection [254, 255]. The Bsoft code was developed for the analysis of a set of cryotomography data, which are characterized by a low contrast and a high noise level [256]. Bsoft employs back projection and the reciprocal space algorithm. Another code package, XMIPP [257], is, in the view of the authors of Ref. [258], more efficient than the filtered back projection technique. Software intended for the processing of nanodimensional TXM images is constantly refined, and considerable recent progress has been achieved [259, 260].

The fields of application of the absorption and phase contrast tomographies are quite broad. Special mention should be made of soft tissue studies conducted using cryogenic tomography [11]. This approach came into use in biological investigations, where determining the chemical composition of a sample ranks next to obtaining a high X-ray absorption contrast, so as to eliminate the emergence of artifacts introduced by sample coloration. Since the sample is not scanned in the course of data collection, a TXM permits carrying out tomography at cryogenic temperatures with the use of an appropriate cryostat [261].

Another field of microtomography application comprises materials science [15], including studies of fuel cells and batteries [262–267], integrated circuits [268, 269], porous structures [270, 271] (see Fig. 24), alloys [272], crystals [72], and cement [273].

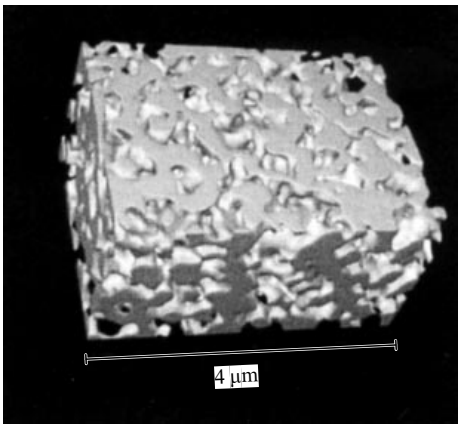

Figure 24. Image of a porous structure of small volume ($2 \times 3 \times 4$ μm^3) obtained by way of 3D reconstruction of a gold wire [270].

Obviously, the combination of chemical information and a high spatial resolution in three dimensions is central to all STXM tomographic approaches. It should not be forgotten, nevertheless, that STXMs use scanning and are rather 'slow' in comparison with TXMs. However, the main advantage of STXM tomography over the TXM approach is the possibility of extracting information about the internal features of the chemical sample composition, i.e., the combination of microscopy and NEXAFS spectroscopy [7].

Recently, Zhu et al. [274] demonstrated the feasibility of constructing polarization-dependent 3D images of nanoobjects along with spectrotomographic images. A sodium titanate nanotape was selected as an object.

9. Conclusions. Outlook and inferences

X-ray microscopy has become a conventional method that is frequently used. It has opened up unprecedented possibilities for the study of diverse complicated materials of various origins. The popularity of the method is due to the keen scientific interest in the execution of noninvasive measurements in the investigation of internal nanodimensional properties of natural or artificial materials.

TXM and STXM methods have always been regarded as complementary; both microscopies are about equally popular, and each offers significant advantages of its own. This viewpoint is likely to persist in the near future. STXMs will always possess a distinct advantage in the investigation of trace element concentrations, in the capacity to promptly move from a large field of view to a small one and to retain constant magnification even when the X-ray radiation energy is changed, and in the capacity of object imaging for a radiation dose close to the theoretical minimum. On the other hand, TXMs are going through a period of technical improvement, advancing to an energy range of several keV and to cryomicroscopy. In concert with basic conventional procedures of multiplexed data acquisition, this strengthens its leading position in tomography, in which X-ray transition microscopy is becoming an ordinary experimental technique. A new trend is the integration of a TXM and an STXM into one instrument with the possibility of switching between these two kinds of microscopy [275].

Another modern trend concerns with studies involving two complementary methods with the subsequent integration of the data sets for constructing an informative composite image. A recent example of the image correlation concept is the combination of soft X-ray tomography and light fluorescence microscopy [276].

There are supposedly two avenues for the development of the experimental basis of X-ray microscopy: development of commercially available laboratory tomographic systems (an example is provided by Xradia activities), and construction of a multimodal analytical platform that combines different techniques, namely, X-ray transmission microscopy, NEXAFS spectroscopy, methods for recording secondary processes (X-ray fluorescence and secondary electrons), optical fluorescence, etc. The possibility of combining different analytical methods in one experiment is a unique advantage of X-ray microscopy.

Evidently, one of the main tasks in the years to come will be the development of advanced X-ray optics which suppress

the X-ray background and overcome the depth-of-focus limitations in tomography. Soft X-ray optics provide a spatial resolution of about 10 nm and in doing so shorten the depth of focus to about 100 nm in the 'water window'. Hard X-ray radiation provides excellent structural, elemental, and chemical sensitivities and possesses a high penetrability. These properties are particularly suited to *in situ* and *in operando* investigations, which are hard or impossible to perform with the exploitation of other techniques (for instance, electron microscopy).

Modern hard X-ray microscopes possess a spatial resolution of up to several dozen nanometers. Nevertheless, of significance for a broad range of scientific problems (elucidation of the structure–functionality relationship) is bringing the spatial resolution to a nanometer level. Recent years have seen certain progress in the fabrication of multilayer Laue lenses capable of producing a linear nanodimensional focus with an efficiency of about 70%. Focusing to a 'point' requires two crossed lenses [277], which complicates the microscope alignment and may entail an impairment of the optical system efficiency. The way out will be found when attempts to make a circular multilayer Laue lens meet with success. However, the focusing efficiency may approach 100% with the use of a nonabsorbing phase-shifting circular FZP with a parabolic (i.e., kinoform) zone profile. So far, these profiles have been extremely hard to realize using the existing lithography techniques.

Among the main features of X-ray microscopy is the continual improvement in X-ray electronic detectors, projection and energy resolutions. Chemical information with a high spatial resolution may be an aid in the development and synthesis of hierarchical functional materials. The possibility of a multidimensional combination of nanolevel spatial resolution with chemical and temporal resolution is one of the greatest prospects for future studies of matter. Ultrafast femtosecond X-ray sources will add, along with high brightness, a fundamental magnetic time scale: it is not unlikely that the imaging of spin dynamics will be realized by single-pulse object irradiation. In this connection, one may envisage the development and analysis of new advanced magnetic materials for the discovery of a great diversity of interactions and their use in applications.

Despite its popularity, modern X-ray microscopy invites further improvement. X-ray microscopy may become a routine technique for investigating condensed media after achieving progress in the quality of experimental data by way of improving research sample preparation, microscope optics, data collection strategy and image reconstruction methods, as well as in the construction of a complete X-ray–matter interaction model.

References

1. Lider V V, Kovalchuk M V *Crystallogr. Rep.* **58** 769 (2013); *Kristallografiya* **58** 764 (2013)
2. Lider V V *Phys. Usp.* **58** 365 (2015); *Usp. Fiz. Nauk* **185** 393 (2015)
3. Howells M, Jacobsen C, Warwick T, in *Science of Microscopy* (Eds P W Hawkes, J C H Spence) Vol. 2 (New York: Springer, 2007) p. 835
4. Kirz J, Jacobsen C *J. Phys. Conf. Ser.* **186** 012001 (2009)
5. Kaulich B et al. *J. Phys. Condens. Matter* **23** 083002 (2011)
6. Behrens S, Kappler A, Obst M *Environ. Microbiol.* **14** 2851 (2012)
7. Obst M, Schmid G *Meth. Mol. Biol.* **1117** 757 (2014)
8. Sakdinawat A, Attwood D *Nature Photon.* **4** 840 (2010)
9. Andrews J C et al. *Microsc. Res. Tech.* **74** 671 (2011)
10. Sedlmair J *Soft X-Ray Spectromicroscopy of Environmental and Biological Samples* (Göttingen Ser. in X-Ray Physics, Vol. 7) (Göttingen: Universitätsverlag, 2011)
11. Carzaniga R et al. *Protoplasma* **251** 449 (2014)
12. Yoon T H *Appl. Spectrosc. Rev.* **44** 91 (2009)
13. Holt M et al. *Annu. Rev. Mater. Res.* **43** 183 (2013)
14. Chae S et al. *Int. J. Concr. Struct. Mater.* **7** 95 (2013)
15. Lavery L L et al. *Microsc. Today* **22** 16 (2014)
16. Hitchcock A P, Toney M F *J. Synchrotron Radiat.* **21** 1019 (2014)
17. Lawrence J R et al. *J. Microsc.* **261** 130 (2016)
18. Hitchcock A P et al. *Aust. J. Chem.* **58** 423 (2005)
19. Hitchcock A P et al., in *Proteins at Interfaces III. State of the Art* (ACS Symp. Ser., Vol. 1120, Eds T Horbett, J L Brash, W Norde) (Washington, DC: American Chemical Society, 2012) p. 731
20. Fischer P, Im M-Y *IEEE Photon. J.* **2** 260 (2010)
21. Fischer P *IEEE Trans. Magn.* **51** 1 (2015)
22. Kuch W et al., in *Magnetic Microscopy of Layered Structures* (Springer Ser. in Surface Sciences, Vol. 57) (Berlin: Springer-Verlag, 2015) p. 189
23. Moffet R C, Tivanski A V, Gilles M K, in *Fundamentals and Applications in Aerosol Spectroscopy* (Eds R Signorell, J P Reid) (Boca Raton, FL: CRC Press, Taylor & Francis, 2010) p. 420
24. Thieme J et al. *J. Synchrotron Radiat.* **17** 149 (2010)
25. Hitchcock A P, Toney M F *J. Synchrotron Radiat.* **21** 1019 (2014)
26. Niemann B, Rudolph D, Schmahl G *Appl. Opt.* **15** 1883 (1976)
27. Kenney J M et al. *Nucl. Instrum. Meth. Phys. Res.* **222** 37 (1984)
28. Hertz H M et al. *J. Struct. Biol.* **177** 267 (2012)
29. Merkle A, Gelb J *Microsc. Microanal.* **19** 1314 (2013)
30. Müller M et al. *Opt. Express* **22** 23489 (2014)
31. Tkachuk A et al. *Z. Kristallogr.* **222** 650 (2007)
32. Feser M et al. *Meas. Sci. Technol.* **19** 094001 (2008)
33. Epting W K, Gelb J, Litster S *Adv. Funct. Mater.* **22** 555 (2012)
34. Jeon S Y et al. *Yonsei Med. J.* **49** 337 (2008)
35. Kilcoyne A L et al. *J. Synchrotron Radiat.* **10** 125 (2003)
36. Baez A V *J. Opt. Soc. Am.* **42** 756 (1952)
37. Yin G-C et al. *Appl. Phys. Lett.* **89** 221122 (2006)
38. Kirz J, Jacobsen C, Howells M *Q. Rev. Biophys.* **28** 33 (1995)
39. Attwood D *Soft X-Rays and Extreme Ultraviolet Radiation: Principles and Applications* (Cambridge: Cambridge Univ. Press, 1999)
40. Michette A G *Optical Systems for Soft X-Rays* (New York: Plenum Press, 1986); Translated into Russian: *Optika Myagkogo Rentgenovskogo Izlucheniya* (Moscow: Mir, 1989)
41. Wu S-R, HwuY, Margaritondo G *Materials* **5** 1752 (2012)
42. Awaji M et al. *J. Synchrotron Radiat.* **9** 125 (2002)
43. Takeuchi A et al. *IPAP Conf. Ser.* **7** 360 (2006)
44. Yun W et al. *Rev. Sci. Instrum.* **70** 2238 (1999)
45. Rehbein S et al. *AIP Conf. Proc.* **1365** 32 (2011)
46. Takeuchi A, Suzuki Y Takano H *J. Synchrotron Radiat.* **9** 115 (2002)
47. Kirz J, Attwood D, in *X-Ray Data Booklet* (Berkeley, CA: Lawrence Berkeley National Laboratory, 2001) p. 4-28
48. Liu Y et al. *Opt. Lett.* **37** 3708 (2012)
49. Johansson G A et al. *J. Synchrotron Radiat.* **14** 395 (2007)
50. Andrews J C et al. *Microsc. Microanal.* **16** 327 (2010)
51. Chen Y-T et al. *Nanotechnology* **19** 395302 (2008)
52. Chao W et al. *Opt. Lett.* **28** 2019 (2003)
53. Chao W et al. *Nature* **435** 1210 (2005)
54. Keskinbora K et al. *Opt. Express* **21** 11747 (2013)
55. Feng Y et al. *J. Vac. Sci. Technol. B* **25** 2004 (2007)
56. Werner S et al. *Microelectron. Eng.* **87** 1557 (2010)
57. Vila-Comamala J et al. *Opt. Express* **19** 175 (2011)
58. Chang C, Sakdinawat A *Nature Commun.* **5** 4243 (2014)
59. Rudolph D, Niemann B, Schmahl G *Proc. SPIE* **316** 103 (1982)
60. Mayer M et al. *Ultramicroscopy* **111** 1706 (2011)
61. Pratsch C et al. *Opt. Express* **22** 30482 (2014)
62. Tamura S et al. *J. Synchrotron Radiat.* **9** 154 (2002)
63. Keskinbora K et al. *Opt. Express* **22** 18440 (2014)
64. Sanli U T et al. *Proc. SPIE* **9592** 95920F (2015)
65. Düvel A, Rudolph D, Schmahl G *AIP Conf. Proc.* **507** 607 (2000)
66. Golant K M et al. *Appl. Opt.* **46** 5964 (2007)
67. Koyama T et al. *Rev. Sci. Instrum.* **83** 013705 (2012)
68. Selin M et al. *Opt. Lett.* **40** 2201 (2015)
69. Heck J M et al. *J. X-Ray Sci. Technol.* **8** 95 (1998)
70. Schmahl G et al. *Optik* **93** 95 (1993)

71. Niemann B, Rudolph D, Schmahl G *Opt. Commun.* **12** 160 (1974)
72. Chen J et al. *Appl. Phys. Lett.* **92** 233104 (2008)
73. Guttmann P et al. *J. Phys. Conf. Ser.* **186** 012064 (2009)
74. Sorrentino A et al. *J. Synchrotron Radiat.* **22** 1112 (2015)
75. Merkle A, Gelb J, Lavery L *Microsc. Microanal.* **19** 1314 (2013)
76. Benk M et al. *Opt. Lett.* **33** 2359 (2008)
77. Zeng X et al. *Appl. Opt.* **47** 2376 (2008)
78. Berglund M et al. *J. Microsc.* **197** 268 (2000)
79. Hertz H M et al. *J. Struct. Biol.* **177** 267 (2012)
80. Legall H et al. *Opt. Express* **20** 18362 (2012)
81. Marschall F et al. *J. Phys. Conf. Ser.* **499** 012007 (2014)
82. Vogt U et al. *Opt. Lett.* **31** 1465 (2006)
83. Wessels P et al. *J. Phys. Conf. Ser.* **499** 012009 (2014)
84. Jefimovs K et al. *J. Synchrotron Radiat.* **15** 106 (2008)
85. Kirz J et al. *Nucl. Instrum. Meth. Phys. Res. B* **87** 92 (1994)
86. Abraham-Peskir J V et al. *Med. Sci. Res.* **26** 663 (1998)
87. Magowan C et al. *Proc. Natl. Acad. Sci. USA* **94** 6222 (1997)
88. Abraham-Peskir J V *Eur. J. Protistology* **34** 51 (1998)
89. Williams S et al. *J. Microsc.* **2** 155 (1993)
90. Wu H R et al. *J. Phys. D* **45** 242001 (2012)
91. Meyer-Ilse W et al. *J. Microsc.* **201** 395 (2001)
92. van Schooneveld M M et al. *Small* **7** 804 (2011)
93. Hertz H M et al. *Chem. Geolog.* **329** 26 (2012)
94. Liao Z et al. *Adv. Eng. Mater.* **16** 486 (2014)
95. Nelson J et al. *J. Am. Chem. Soc.* **134** 6337 (2012)
96. Knehr K W et al. *J. Electrochem. Soc.* **162** A255 (2015)
97. Blokhin M A *Fizika Rentgenovskikh Luchei* (The Physics of X-Rays) (Moscow: GITTL, 1957)
98. Zernike F *Z. Tech. Physik.* **16** 454 (1935)
99. Schmahl G et al. *Rev. Sci. Instrum.* **66** 1282 (1995)
100. Neuhäusler U et al. *J. Phys. D* **36** A79 (2003)
101. Schneider G et al., in *X-Ray Microscopy and Spectromicroscopy. Statue Report from the Fifth Intern. Conf., Würzburg, August 19 – 23, 1996* Vol. 1 (Eds J Thieme et al.) (Berlin: Springer, 1998) p. 111
102. Kim G B et al. *Microsc. Res. Tech.* **71** 639 (2008)
103. Chien C C et al. *Biotechnol. Adv.* **31** 375 (2013)
104. Lee O et al. *Microsc. Res. Tech.* **73** 1110 (2010)
105. Chao S C et al. *J. Electrochem. Soc.* **158** A1335 (2011)
106. Neuhäusler U, Schneider G *Microelectron. Eng.* **83** 1043 (2006)
107. Sakdinawat A, Liu Y *Opt. Express* **16** 1559 (2008)
108. Chen Y-T et al. *Opt. Lett.* **36** 1269 (2011)
109. Wilhein T et al. *Appl. Phys. Lett.* **78** 2082 (2001)
110. Kaulich B et al. *J. Opt. Soc. Am. A* **19** 797 (2002)
111. Feser M et al. *Proc. SPIE* **4499** 117 (2001)
112. Chang C et al. *Appl. Opt.* **41** 7384 (2002)
113. Chang C et al. *Opt. Lett.* **31** 1564 (2006)
114. Bertilson M C et al. *Appl. Phys. Lett.* **92** 064104 (2008)
115. Nakamura T, Chang C *Phys. Rev. A* **83** 043808 (2011)
116. Morrison G R *Proc. SPIE* **1741** 186 (1993)
117. Thibault P et al. *Phys. Rev. A* **80** 043813 (2009)
118. Hornberger B et al. *J. Synchrotron Radiat.* **15** 355 (2008)
119. Feser M et al. *AIP Conf. Proc.* **507** 367 (2000)
120. Feser M et al. *J. Physique IV* **104** 529 (2003)
121. Feser M et al. *Nucl. Instrum. Meth. Phys. Res. A* **565** 841 (2006)
122. Kourousias G et al. *X-Ray Spectrom.* **44** 163 (2015)
123. Morrison G R, Browne M T *Rev. Sci. Instrum.* **63** 611 (1992)
124. Vogt S et al. *Ultramicroscopy* **87** 25 (2001)
125. Chapman H N, Jacobsen C, Williams S *Rev. Sci. Instrum.* **66** 1332 (1995)
126. Gianoncelli A et al. *Appl. Phys. Lett.* **89** 251117 (2006)
127. Morrison G R et al. *J. Physique IV* **104** 547 (2003)
128. Menzel A et al. *J. Phys. Conf. Ser.* **186** 012054 (2009)
129. de Jonge M D et al. *J. Phys. Conf. Ser.* **186** 012006 (2009)
130. Hornberger B, Feser M, Jacobsen C *Ultramicroscopy* **107** 644 (2007)
131. de Jonge M D et al. *Phys. Rev. Lett.* **100** 163902 (2008)
132. Rehr J J, Albers R C *Rev. Mod. Phys.* **72** 621 (2000)
133. Hähner G *Chem. Soc. Rev.* **35** 1244 (2006)
134. Ade H, Hitchcock A P *Polymer* **49** 643 (2008)
135. Lehmann J et al., in *Biophysico-Chemical Processes Involving Natural Nonliving Organic Matter in Environmental Systems* (Eds N Senesi, B Xing, P M Huang) (Hoboken, NJ: Wiley, 2009) p. 729
136. Miot J et al. *Geobiology* **9** 459 (2011)
137. Hitchcock A P et al. *Ultramicroscopy* **88** 33 (2001)
138. Koprinarov I N et al. *J. Phys. Chem. B* **106** 5358 (2002)
139. Ade H, Urquhart S, in *Chemical Applications of Synchrotron Radiation* (Adv. Ser. in Phys. Chem., Vol. 12, Ed. T-K Sham) (Singapore: World Scientific, 2002) p. 285
140. Hitchcock A P et al. *J. Biomater. Sci. Polym. Ed.* **13** 919 (2002)
141. Jacobsen C et al. *J. Microsc.* **197** 173 (2000)
142. Hitchcock A P *J. Synchrotron Radiat.* **8** 66 (2001)
143. Jacobsen C et al. *Surf. Rev. Lett.* **9** 185 (2002)
144. King P L et al. *J. Vac. Sci. Technol. A* **7** 3301 (1989)
145. Lerotic M et al. *J. Electron Spectrosc. Relat. Phenom.* **144 – 147** 1137 (2005)
146. Jacobsen C *Trends Cell Biol.* **9** 44 (1999)
147. Ade H, Stoll H *Nature Mater.* **8** 281 (2009)
148. Obst M et al. *Geochim. Cosmochim. Acta* **73** 4180 (2009)
149. Hitchcock A P et al. *Geobiology* **7** 432 (2009)
150. Dynes J J et al. *Sci. Total Environ.* **369** 369 (2006)
151. Salome M et al. *Am. Inst. Phys. Conf. Proc.* **507** 178 (2000)
152. Chan C S et al. *ISME J.* **5** 717 (2011)
153. Yangquanwei Z, Neethirajan S, Karunakaran C *Nanoscale Res. Lett.* **8** 463 (2013)
154. Sun S et al. *Int. J. Mol. Sci.* **15** 23604 (2014)
155. Cosmidis J et al. *Acta Biomater.* **12** 260 (2015)
156. Urquhart S G et al. *J. Electron Spectrosc. Relat. Phenom.* **100** 119 (1999)
157. Hitchcock A P et al. *J. Electron Spectrosc. Relat. Phenom.* **144 – 147** 259 (2005)
158. Zhang W et al. *Macromolecules* **35** 8029 (2002)
159. Ade H et al. *Polymer* **36** 1843 (1995)
160. Si M et al. *Macromolecules* **39** 4793 (2006)
161. McNeill C R et al. *Macromolecules* **40** 3263 (2007)
162. Takekoh R et al. *Macromolecules* **38** 542 (2005)
163. Muntean L et al. *J. Vac. Sci. Technol. B* **23** 1630 (2005)
164. Araki T et al. *J. Biomat. Sci. Polym. E* **16** 611 (2005)
165. Croll L M, Stöver H D H, Hitchcock A P *Macromolecules* **38** 2903 (2005)
166. Wang J et al. *J. Synchrotron Radiat.* **14** 181 (2007)
167. Iwata N et al. *Micron* **37** 290 (2006)
168. Rightor E G et al. *Macromolecules* **35** 5873 (2002)
169. Leung B O et al. *Langmuir* **25** 13332 (2009)
170. Mitchell G E et al. *Polymer* **52** 3956 (2011)
171. Arrua R D et al. *Anal. Chem.* **86** 2876 (2014)
172. Karunakaran C et al. *PLoS One* **10** e0122959 (2015)
173. Mitchell G E et al. *Macromolecules* **35** 1336 (2002)
174. Fujii S et al. *J. Am. Chem. Soc.* **127** 16808 (2005)
175. Fujii S et al. *Langmuir* **25** 2588 (2009)
176. Felten A et al. *Nano Lett.* **7** 2435 (2007)
177. Bittencourt C et al. *Beilstein J. Nanotechnol.* **3** 345 (2012)
178. Bittencourt C, Krüger P, Lagos M J *Beilstein J. Nanotechnol.* **3** 789 (2012)
179. Bittencourt C et al. *Chem. Phys. Lett.* **587** 85 (2013)
180. Boesenberg U et al. *Chem. Mater.* **25** 1664 (2013)
181. Berejnov V et al. *Phys. Chem. Chem. Phys.* **14** 4835 (2012)
182. Li L et al. *Nature Commun.* **6** 6883 (2015)
183. Yu Y-S et al. *Adv. Energy Mater.* **5** 1402040 (2014)
184. Gallaway J W et al. *J. Electrochem. Soc.* **161** A275 (2014)
185. Cody G D et al. *Energy Fuels* **9** 153 (1995)
186. Braun A et al. *Fuel* **83** 997 (2004)
187. Lawrence J R et al. *Appl. Environ. Microbiol.* **69** 5543 (2003)
188. Solomon D et al. *Sci. Total Environ.* **438** 372 (2012)
189. Chen C et al. *Environ. Sci. Technol.* **48** 6678 (2014)
190. Cody G D *AIP Conf. Proc.* **507** 307 (2000)
191. Buckley C J et al. *Holzforschung* **56** 215 (2002)
192. Boyce C K et al. *Int. J. Plant Sci.* **164** 691 (2003)
193. Karunakaran C et al., Saskatoon. Canadian Light Source 50 (2010)
194. Oraji R et al., Saskatoon. Canadian Light Source 118 (2013)
195. Myneni S C B, Tokunaga T K, Brown G E (Jr.) *Science* **278** 1106 (1997)
196. Miot J et al. *Geochim. Cosmochim. Acta* **73** 696 (2009)
197. Koehl A et al. *APL Mater.* **1** 042102 (2013)
198. de Smit E et al. *Nature* **456** 222 (2008)
199. Wang J, Chen-Wiegart Y K, Wang J *Nature Commun.* **5** 4570 (2014)
200. Henzler K et al. *Nano Lett.* **13** 824 (2013)
201. Chueh W C et al. *Nano Lett.* **13** 866 (2013)

202. Ovchinnikov S G *Phys. Usp.* **42** 779 (1999); *Usp. Fiz. Nauk* **169** 869 (1999)
203. Fetisov G V *Sinkhrotronnoe Izluchenie: Metody Issledovaniya Struktury Veshchestv* (Synchrotron Radiation: Methods for Material Structure Investigation) (Moscow: Fizmatlit, 2007)
204. Schütz G et al. *Phys. Rev. Lett.* **58** 737 (1987)
205. Chen C T et al. *Phys. Rev. B* **42** 7262(R) (1990)
206. Stöhr J et al. *Science* **259** 658 (1993)
207. Fischer P et al. *J. Phys. D* **31** 649 (1998)
208. Fischer P et al. *J. Appl. Phys.* **89** 7159 (2001)
209. Fischer P et al. *IEEE Trans. Magn.* **38** 2427 (2002)
210. Fischer P et al. *J. Magn. Magn. Mater.* **286** 311 (2005)
211. Im M-Y et al. *Appl. Phys. Lett.* **95** 182504 (2009)
212. Gräfe J et al. *Phys. Rev. B* **93** 014406 (2016)
213. Meier G et al. *Phys. Rev. Lett.* **98** 187202 (2007)
214. Bryan M T et al. *J. Appl. Phys.* **103** 07D909 (2008)
215. Im M-Y et al. *Phys. Rev. Lett.* **102** 147204 (2009)
216. Im M-Y et al. *J. Phys. Condens. Matter* **24** 024203 (2012)
217. Fischer P et al. *J. Magn. Magn. Mater.* **310** 2689 (2007)
218. Kasai S et al. *Phys. Rev. Lett.* **101** 237203 (2008)
219. Mesler B L et al. *J. Appl. Phys.* **111** 07D311 (2012)
220. Van Waeyenberge B et al. *Nature* **444** 461 (2006)
221. Bocklage L et al. *Phys. Rev. B* **78** 180405(R) (2008)
222. Chou K W et al. *J. Appl. Phys.* **99** 08F305 (2006)
223. Strachan J P et al. *Phys. Rev. Lett.* **100** 247201 (2008)
224. Acremann Y et al. *Phys. Rev. Lett.* **96** 217202 (2006)
225. Lüning J et al. *Phys. Rev. B* **67** 214433 (2003)
226. Ade H, Hsiao B *Science* **262** 1427 (1993)
227. Kaznatcheev K V et al. *Phys. Rev. E* **76** 061703 (2007)
228. Urquhart S G, Lanke U D, Fu J *Int. J. Nanotechnol.* **5** 1138 (2008)
229. Croll L M et al. *J. Synchrotron Radiat.* **10** 265 (2003)
230. Kowarik S et al. *J. Phys. Chem. C* **114** 13061 (2010)
231. Collins B A et al. *Nature Mater.* **11** 536 (2012)
232. Watts B, Schuettfort T, McNeill C R *Adv. Funct. Mater.* **21** 1121 (2011)
233. Bräuer B et al. *Chem. Mater.* **22** 3693 (2010)
234. Hub C et al. *J. Mater. Chem.* **20** 4884 (2010)
235. Smith A P, Ade H *Appl. Phys. Lett.* **69** 3833 (1996)
236. Rousseau M-E et al. *J. Am. Chem. Soc.* **129** 3897 (2007)
237. Smith A P et al. *Macromol. Rapid Commun.* **19** 557 (1998)
238. Kaulich B et al. *J. R. Soc. Interface* **6** S641 (2009)
239. Ryan C G et al. *J. Phys. Conf. Ser.* **499** 012002 (2014)
240. Gianoncelli A et al. *J. Phys. Conf. Ser.* **463** 012004 (2013)
241. Pascolo L et al. *Part. Fibre Toxicol.* **8** 7 (2011)
242. Gianoncelli A et al. *J. Phys. Conf. Ser.* **425** 182001 (2013)
243. Poitry-Yamate C et al. *J. Neurosci. Res.* **91** 1050 (2013)
244. Poitry-Yamate C et al. *J. Phys. Conf. Ser.* **463** 012003 (2013)
245. Gianoncelli A et al. *X-Ray Spectrom.* **42** 316 (2013)
246. Novak S et al. *Environ. Sci. Technol.* **47** 5400 (2013)
247. Pascolo L et al. *Sci. Rep.* **3** 1123 (2013)
248. Haddad W S et al. *Science* **266** 1213 (1994)
249. Lehr J *Optik* **104** 166 (1997)
250. Lavery L et al. *Microsc. Microanal.* **21** 131 (2015)
251. Kremer J R, Mastronarde D N, McIntosh J R *J. Struct. Biol.* **116** 71 (1996)
252. Castano-Diez D et al. *J. Struct. Biol.* **170** 117 (2010)
253. Parkinson D Y et al. *Meth. Mol. Biol.* **950** 457 (2013)
254. Kak A C, Slaney M *Principles of Computerized Tomographic Imaging* (New York: IEEE Press, 1988)
255. Frank J et al. *J. Struct. Biol.* **116** 190 (1996)
256. Heymann J B, Belnap D M *J. Struct. Biol.* **157** 3 (2007)
257. Sorzano C O S et al. *J. Struct. Biol.* **148** 194 (2004)
258. Parkinson D Y et al. *J. Struct. Biol.* **162** 380 (2008)
259. Liu Y et al. *J. Synchrotron Radiat.* **19** 281 (2012)
260. Kumar A S et al. *J. Appl. Phys.* **117** 183102 (2015)
261. Le Gros M A, McDermott G, Larabell C A *Curr. Opin. Struct. Biol.* **15** 593 (2005)
262. Litster S et al. *Fuel Cells* **13** 935 (2013)
263. Cronin J S et al. *Power Sources* **233** 174 (2013)
264. Eastwood D S et al. *Adv. Energy Mater.* **4** 1300506 (2014)
265. Liu Z et al. *J. Power Sources* **227** 267 (2013)
266. Nelson Weker J et al. *Energy Environ. Sci.* **7** 2771 (2014)
267. Wang J *ChemElectroChem.* **2** 329 (2014)
268. Levine Z H et al. *J. Appl. Phys.* **87** 4483 (2000)
269. Wang S et al., in *Proc. of the 28th Intern. Symp. for Testing and Failure Analysis, 3–7 November 2002, Phoenix, AZ* (Ed. C Boit) (Materials Park, OH: ASM Intern., 2002) p. 227
270. Chen C K et al. *Appl. Phys. Lett.* **96** 043122 (2010)
271. Hilhorst J et al. *Langmuir* **28** 3614 (2012)
272. Chen-Wiegart Y K et al. *Acta Mater.* **61** 1118 (2013)
273. Monteiro P J M et al. *Cement Concrete Composit.* **31** 577 (2009)
274. Zhu X et al. *J. Phys. Chem. C* **119** 24192 (2015)
275. Kaulich B et al. *IPAP Conf. Ser.* **7** 22 (2006)
276. Smith E A et al. *Ultramicroscopy* **143** 33 (2014)
277. Nazaretski E et al. *Rev. Sci. Instrum.* **84** 033701 (2013)